

Modeling the Transport and Dispersion of Volcanic Co-PDC Ash Clouds Using NAME: An Evaluation of Source Geometry and Mass Eruption Rate

M. Hagenbourger¹ , F. M. Beckett² , T. J. Jones¹ , and S. L. Engwell³ 

¹Lancaster Environment Centre, Lancaster University, Lancaster, UK, ²Met Office, Exeter, UK, ³British Geological Survey, The Lyell Centre, Edinburgh, UK

Key Points:

- We explored the range of source parameters suitable for a co-PDC plume and the sensitivity of transport and dispersion model simulations
- Variations in our source geometries (area and aspect ratio) and metrological conditions used have negligible effects on ash dispersion
- Ash cloud simulation results are sensitive to the co-PDC plume height and associated mass eruption rate

Supporting Information:

Supporting Information may be found in the online version of this article.

Correspondence to:

M. Hagenbourger,
m.hagenbourger@lancaster.ac.uk

Citation:

Hagenbourger, M., Beckett, F. M., Jones, T. J., & Engwell, S. L. (2026). Modeling the transport and dispersion of volcanic co-PDC ash clouds using NAME: An evaluation of source geometry and mass eruption rate. *Journal of Geophysical Research: Atmospheres*, 131, e2025JD044031. <https://doi.org/10.1029/2025JD044031>

Received 27 APR 2025

Accepted 21 FEB 2026

Abstract Pyroclastic density currents (PDCs) are gravity currents that frequently form during explosive volcanic eruptions. These ground-hugging density currents consist of high-temperature mixtures of pyroclasts (e.g., ash, pumice), lithics, and gas. They have the potential to generate co-PDC plumes, which detach from the underlying PDC as they buoyantly rise into the atmosphere. Co-PDC plumes, composed of fine-grained ash particles and hot gas, can reach heights of tens of kilometers, potentially dispersing large volumes of ash over continental scale areas, impacting the environment, and posing a risk to aviation. Owing to their formation mechanism, co-PDCs have unique characteristics, such as fine particle sizes (e.g., <90 μm) and a high-aspect ratio, irregular-shaped, source geometry. Here, we consider how the release of ash into the atmosphere from a co-PDC plume may differ to that from a typical Plinian eruption column, and the implications for operational modeling of the resulting ash cloud for the provision of advice to the aviation industry. We use the Numerical Atmospheric-Dispersion Modelling Environment (NAME), which is used by the London Volcanic Ash Advisory Centre. We performed a sensitivity analysis to determine which co-PDC source parameters are important for modeling the associated ash clouds. We show that variations in the source geometry, that is, the total area and aspect ratio, have a minor impact after the first ~6 hr in the atmosphere.

Plain Language Summary During volcanic eruptions, fast-moving mixtures of hot gas and rock, called pyroclastic density currents (PDCs), can separate into a ground hugging dense current and a buoyant plume that rises into the atmosphere, potentially reaching heights of tens of kilometers. These plumes are called co-PDC plumes. Relative to typical, vent-derived, volcanic ash plumes, they have finer-grained particles and are sourced from irregularly shaped ground regions. Our study applied and analyzed a selection of co-PDC source parameters (e.g., source area) to the Numerical Atmospheric-Dispersion Modelling Environment (NAME) used by the London Volcanic Ash Advisory Centre. Changes in the source geometry, that is, the ground shape and the area from where ash particles lift off, only show minor influences on the ash cloud shape, transport and dispersion, and mass of ash in the atmosphere. However, changes in the plume height and the rate at which ash particles are released into the atmosphere highly impact the ash cloud location, its areal coverage, and the mass of ash in the atmosphere. This improved understanding of input parameter importance could be used for future model forecasting of co-PDC ash dispersal.

1. Introduction

Pyroclastic density currents (PDCs) are ground-hugging gravity currents that can occur during an explosive volcanic eruption through eruption column collapse (R. J. Brown & Andrews, 2015; Dellino et al., 2021; Druitt, 1998; Dufek et al., 2015; Giordano & Cas, 2021; T. J. Jones et al., 2023; Lube et al., 2020) or from the collapse of lava dome or flow fronts (Bonadonna, Mayberry, et al., 2002; Calder et al., 1997; Charbonnier & Gertisser, 2008; Michol et al., 2008; Sigurdsson & Carey, 1989; Sulpizio et al., 2010; Ui et al., 1999). They are a multi-phase mixture composed of hot gas and solid particles (e.g., lithics, pumice, ash) that propagate downslope with flow paths that are largely controlled by topography (Andrews & Manga, 2011, 2012; R. J. Brown & Andrews, 2015; Druitt, 1998; Dufek et al., 2015; T. J. Jones et al., 2023; Lube et al., 2020). All PDCs have the potential to generate co-PDC plumes, also known as co-ignimbrites or phoenix clouds (Andrews & Manga, 2011; Bursik & Woods, 1996; Engwell & Eychenne, 2016; Rosi et al., 2006; Sigurdsson & Carey, 1989; Sparks et al., 1997). These secondary plumes are composed of fine-grained particles and gas, which detach from the underlying PDC current by air intrusion and rise vertically by buoyancy (Andrews & Manga, 2011, 2012,

© 2026. Crown copyright and The Author(s). This article is published with the permission of the Controller of HMSO and the King's Printer for Scotland.

This is an open access article under the terms of the [Creative Commons Attribution License](https://creativecommons.org/licenses/by/4.0/), which permits use, distribution and reproduction in any medium, provided the original work is properly cited.

Engwell & Eychenne, 2016; T. J. Jones et al., 2023; Sparks et al., 1997). Within the PDC, particle sedimentation acts to lower the current density, particularly in its uppermost regions, and when below ambient atmospheric density, a plume can form (Andrews & Manga, 2012; Engwell et al., 2016; Woods & Kienle, 1994). These co-PDC plumes rise in the atmosphere until reaching a level of neutral buoyancy and disperse laterally like umbrella clouds, however co-PDCs clouds are typically much smaller (Constantinescu et al., 2021; Mastin & Van Eaton, 2020; Prata et al., 2025; Zidikheri et al., 2017). In some cases, co-PDCs can become inverted downwind and descend to the ground (Engwell & Eychenne, 2016), thus increasing the ground area impacted by the co-PDC. In this contribution, we use the term “plume” to refer to the near-source behavior of the buoyant column, whereas the downwind transport and dispersion of ash is referred to as the “ash cloud”.

Co-PDC plumes and clouds have unique characteristics and are different from typical Plinian eruption columns and their associated ash clouds. For example, co-PDCs typically have a narrower particle size distribution (PSD) and are composed of smaller particles ($<90\ \mu\text{m}$) (Engwell & Eychenne, 2016; Sigurdsson & Carey, 1989). This is because during co-PDC formation and plume lift-off, the coarser (heavier) particles remain in the underlying PDC (Andrews & Manga, 2012; Woods & Kienle, 1994). Similarly, their componentry is mostly juvenile-rich (i.e., composed mainly of volcanic ash) as the denser accessory components such as lithics preferentially remain in the main current (Engwell & Eychenne, 2016; Sigurdsson & Carey, 1989). The plumes lift off from a source geometry i.e. of high aspect ratio (i.e., an irregular, elongated, rectangular ground footprint and not a circular vent). Furthermore, the source area is not necessarily at the eruption vent location as co-PDCs can be generated and lift-off from all parts of the associated PDC, including its entire length (Andrews & Manga, 2011; Engwell & Eychenne, 2016; Sparks et al., 1986, 1997).

Some numerical 1D models have previously been used to model co-PDC plume rise (Calder et al., 1997; Woods & Kienle, 1994; Woods & Wohletz, 1991) and they assume a thermal equilibrium between particles and gas and a well-mixed, homogenous suspension (Engwell et al., 2016; Woods & Wohletz, 1991). Specifically, Calder et al. (1997), Engwell et al. (2016), Sparks et al. (1997) and Woods and Wohletz (1991) adapted steady state column models commonly used for vent-derived plumes to simulate the formation of a co-PDC plume from an underlying PDC. Other studies such as Woods and Kienle (1994) applied a thermal model to simulate small plumes rising as a discrete buoyant thermal rise. Multidimensional models have also been applied to co-PDC plumes. Neri et al. (2002), Neri et al. (2003) mainly investigated the material properties and the multiphase nature of the flow and Herzog and Graf (2010) used a 3D model to highlight the limits of 1D models for co-PDC plumes. Additionally, Engwell et al. (2016) used work from Bursik (2001) and Bursik and Woods (1996) to couple PDC and plume models to understand co-PDC plume formation requirements and the plume heights they can achieve.

Co-PDCs can be generated during an explosive eruption and disperse large volumes of ash over great distances (Engwell & Eychenne, 2016), impacting the environment and potentially aviation (Engwell et al., 2016; Folch et al., 2012; Pardini et al., 2024; Webster et al., 2012; Witham et al., 2012). Despite global applicability and potential impact, relatively little modelling has been performed to consider the implications of the source parameters characteristic of co-PDCs on the downwind location, extent and concentrations of ash in the atmosphere. The Numerical Atmospheric-Dispersion Modelling Environment (NAME) is operationally used by the London Volcanic Ash Advisory Center (VAAC). Here, we perform a set of NAME model runs to systematically evaluate the impact of co-PDC source geometry, the mass eruption rate, and the associated plume height on the modeled transport and dispersion of the volcanic ash cloud. This allows us to determine which co-PDC eruption source parameters (ESPs) are most important for modeling these ash clouds using NAME in an operational setting.

2. Methods

Ash dispersion and transportation modeling were performed using the UK Met Office's NAME model in its Lagrangian configuration. Specifically, here, version NAME III v8.5 was used (Beckett et al., 2020; A. Jones et al., 2007). NAME simulates the transport and dispersion of particles (e.g., particulate matter, volcanic ash, wind-spread diseases, radionuclides, and pollen) in the atmosphere. In NAME, a large number of modeled particles are released into a model environment where they are advected by three-dimensional wind fields, provided by a Numerical Weather Prediction (NWP) model, and dispersed using random walk techniques which account for subgrid turbulent motion in the atmosphere.

In this study, a fictitious volcanic co-PDC plume and its generated ash cloud were modeled. We assumed that a volcanic eruption produced a PDC and generated an associated co-PDC plume. Our model started at the lateral ash injection at the level of neutral buoyancy into the atmosphere and, using NAME, we modeled the transport and dispersion of the ash cloud generated by the co-PDC plume. To understand which ESPs control the atmospheric transport and dispersion of co-PDC ash clouds, we performed 63 systematic NAME model runs (and 231 additional runs for the Supporting Information S1). The particle characteristics, eruption location, eruption start time, duration, and the field proportions (i.e., horizontal grid resolution of 0.1° in Lat and Long) were all kept constant. The source geometry and, thus indirectly, its area and location, were systematically varied. The specific ESPs used are detailed in the following subsections. In all cases, we assumed time homogeneity, meaning that for each model run the parameters did not vary as a function of time (i.e., the source area was a constant value within each run). We assumed an even vertical distribution of particles at the source and no plume overshoot height and thus a reduced complexity, compared to real events observed in nature, for example, for Mount St. Helens on 18th May 1980 (Mastin et al., 2022; Sparks et al., 1986), where the plume height and mass distribution varied during the eruption. In all runs, we also used the wet and dry deposition schemes in NAME to replicate the removal of ash from the atmosphere; for further information, see Dacre et al. (2011), Harvey et al. (2018) and Webster et al. (2012).

2.1. Eruption Timing, Location and Meteorology Data

In this study, we use pre-processed global configured NWP data from the Met Office Unified Model (UM) (Beckett et al., 2020; A. Brown et al., 2012; Davies et al., 2005; Walters et al., 2019). In addition to the weather and turbulence, unresolved mesoscale motions, which are not resolved by the NWP model, are also represented (Webster et al., 2018). We used the global configuration of the UM, which used a standard latitude-longitude coordinate system and provided a global data set with a horizontal resolution with grid lengths of approximately 10 km at mid-latitudes. The vertical resolution decreases with increased altitude; for example, near ground level data sets are available at ~ 0.03 km intervals, whereas at a 30 km altitude this interval reduces to ~ 1.9 km. However, it is also worth noting that the atmosphere tends to be more stable at higher altitudes. These meteorological data sets include the wind speed and direction, temperature, pressure, clouds, precipitation, and the ground topography for each grid cell.

For this project, Hekla volcano in Iceland was selected as the source location; however, our study is not unique to Hekla as we investigate the ash cloud and NAME model sensitivity, and the focus is not on any specific local topographic effects or unique volcano properties. Hekla is situated at 63.98°N , and 19.67°W (Global Volcanism Program, 2024) in the south of Iceland, has a vent elevation of 1,490 m (Global Volcanism Program, 2024), and is 51 km away from the Atlantic Ocean; thus, no interaction with seawater was considered. The release of modeled ash at a given height in the atmosphere was initialized at 09:00 UTC on the 31st January 2022 and particles were emitted for 1 hr. This start time/day was chosen as the wind fields were not extreme and, in general, traveled in the SE direction toward Europe. Figure 1 shows the wind fields on 31st January 2022 at 09:00 UTC (the start of ash release) and 1 hr later at 10:00 UTC (the end of ash release). The wind fields at 0.01 km above ground level (agl) and at 8.5 km agl show large differences, as displayed in Figure 1. Near the surface (0.01 km agl; Figures 1a and 1b), the wind over Iceland was slower than over the ocean. Over Hekla, wind speeds were very low, with a slight orientation toward NE and NW. The wind field at 0.01 km agl was clearly impacted by the ground topography and the coastline. Whereas at higher elevation (8.5 km agl; Figures 1c and 1d) westerly winds were present over Hekla. The vertical wind profile at the source location, including wind direction and wind speed, is provided in Supporting Information S1 (Figure S1) and confirms the above. Although we focus on this date (31st January 2022), as detailed in Section 2.5.1, we also performed a series of supplementary model runs across the eight weather patterns for the North Atlantic and European regions (Neal et al., 2016) to ensure that any results we present are not unique to a specific day/time. The weather patterns defined by Neal et al. (2016) were identified using cluster analysis and represent the range of circulation types in this region, which differ in their characteristics. These additional meteorological conditions and their vertical wind profiles are presented in Supporting Information S1 (Figures S18 to S66).

2.2. Source Geometry and Location

As co-PDCs are derived from ground-hugging PDCs, the source of ash in the atmosphere may not occur from the vent location. Here, the source was always positioned immediately to the east of the volcanic vent in all runs, such

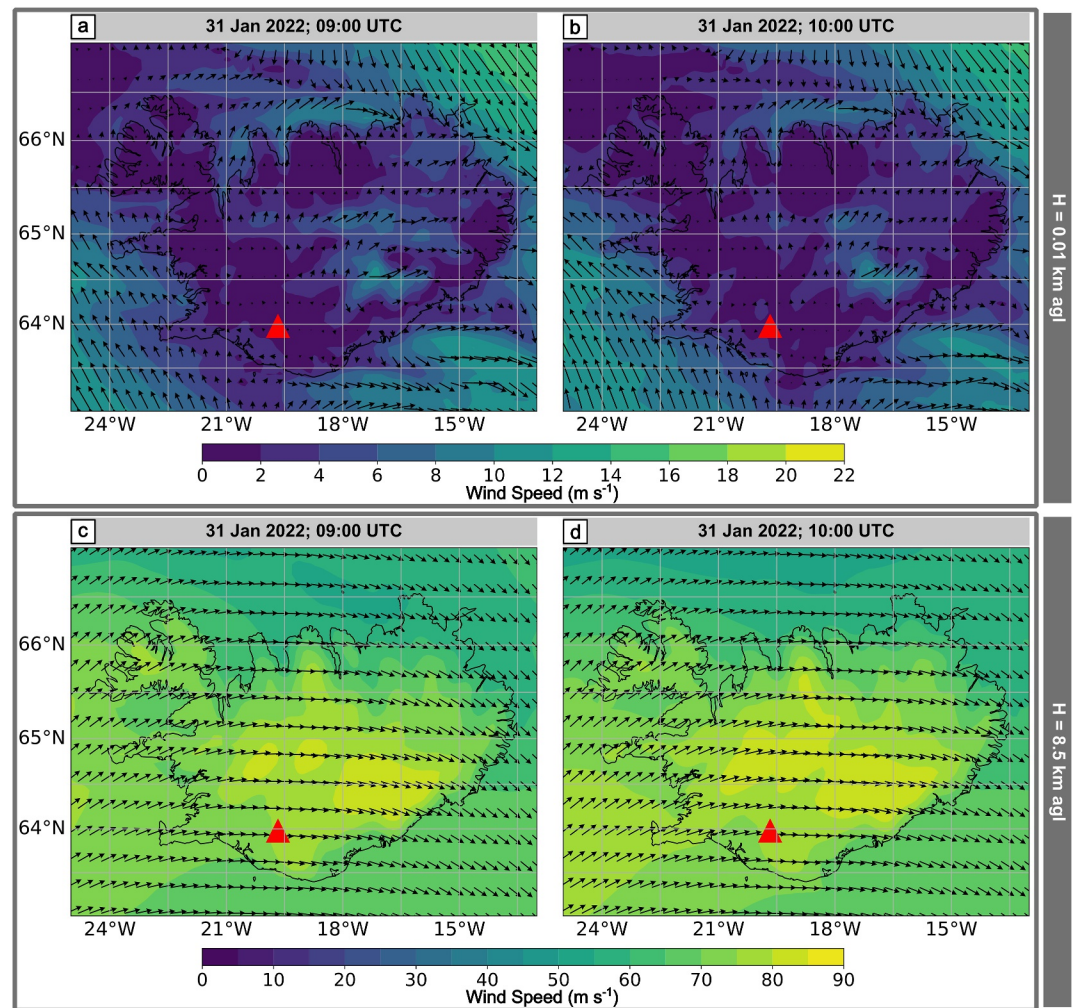


Figure 1. Meteorological data for Iceland on 31st January 2022. The red triangle shows the location of Hekla, where the simulated co-PDC plume is sourced. The top two panels show the wind behavior at 10 m agl elevation at times (a) 09:00 UTC, start of particle release and (b) 10:00 UTC, the end of particle release. The color bar ranges between 0 and 22 m s^{-1} . The wind direction and speed were relatively constant over the 2 hr, although the field was impacted by topography and the coastline. The bottom two panels show the wind field at 8.5 km agl elevation for (c) 09:00 UTC and (d) 10:00 UTC. Only every third arrow is represented to facilitate a better overview. The color bar ranges from 0 to 90 m s^{-1} , and the wind field was relatively homogeneous.

that the meteorological conditions at the source location remained constant between runs. The source geometry, in plan/map view, for the co-PDC plumes simulated here has a rectangular shape with a width, dx , and length, dy , and together these parameters define the source aspect ratio:

$$\alpha = \frac{dx}{dy} \quad (1)$$

All PDCs have the potential to produce co-PDC plumes, which can lift off from the entire underlying PDC (Engwell & Eychenne, 2016; Sparks et al., 1997). To bracket the range of co-PDC source areas likely in nature, we measured the source of the largest and smallest well-documented co-PDCs. Specifically, the 18 May 1980 eruption of Mount St Helens (MSH) generated a large co-PDC with a lift-off from the entire blast area, A , and the 1991 eruption of Unzen generated a relatively small co-PDC plume again, from the entire PDC ground footprint (Engwell et al., 2016; Holasek & Self, 1995; Sparks et al., 1986, 1997; Watanabe et al., 1999). These areas are shown in Figure 2. The area of the blast/deposit and the area of the source geometry are highlighted in dark and light red, respectively. Unzen had a total PDC deposit area of 0.4 km^2 and an aspect ratio of $\alpha = 0.2$. Mount St

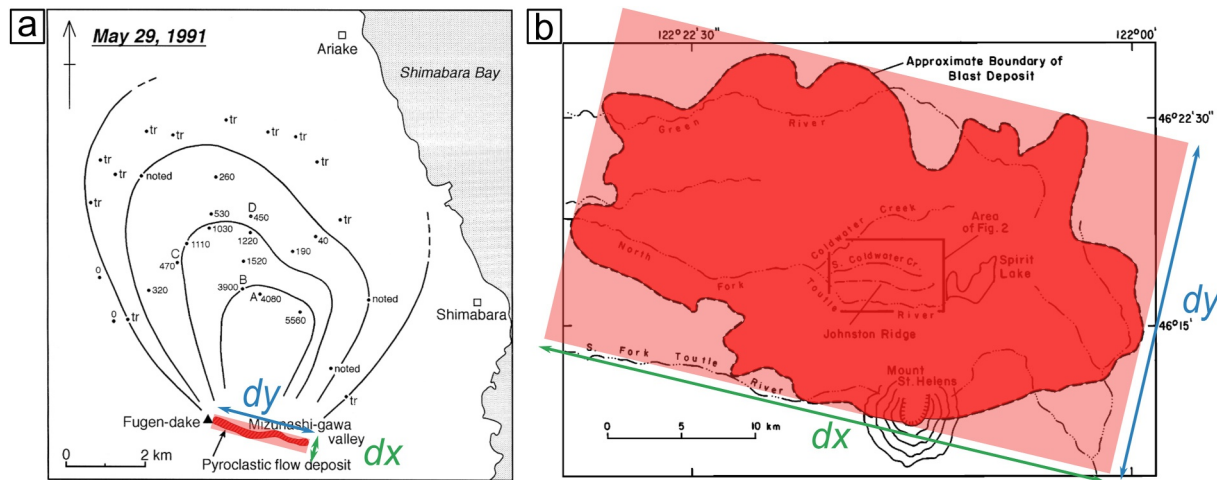


Figure 2. Pyroclastic density current (PDC) deposit area shown in dark red for (a) the 29 May 1991 eruption of Mount Unzen, Japan and (b) the 18 May 1980 eruption of Mount St. Helens, USA. Base maps were taken from Watanabe et al. (1999) with permission from Elsevier and Fisher et al. (1987) with permission from Wiley, respectively, and for (a) the associated co-PDC fallout is shown by the isopach map. The numbers refer to a mass of ash in a unit area (g m^{-2}), where tr = trace of ash-fall deposit. The aspect ratio defining the source geometry, that is, the area of co-PDC lift off, is highlighted in transparent light red. The orientation of dx and dy was defined by the volcano location (dy aligns with the PDC flow/blast direction; dx therefore is perpendicular to the PDC flow direction).

Helens had a blast/PDC deposit area of approximately 619 km^2 and an aspect ratio of $\alpha = 1.7$. The minimum (from Unzen) and maximum (from MSH) observed aspect ratios were used in our numerical experiment as end-member parameters. The PDC flow/blast direction has been defined as dy ; therefore, dx is perpendicular to the PDC flow direction. For each aspect ratio, we varied the area logarithmically between the deposit areas of Unzen and MSH.

The following describes how width and length are calculated using the area and aspect ratio to initialize the model:

$$dx \cdot dy = A \quad (2)$$

With Equation 1, dx :

$$dx = \sqrt{A \cdot \alpha} \quad (3)$$

dy with Equation 1 becomes:

$$dy = \sqrt{\frac{A}{\alpha}} \quad (4)$$

2.3. Eruption Conditions

To determine the maximum height of the co-PDC plumes, H_T , data sets from Aubry et al. (2021), Eychenne and Engwell (2022), Mastin et al. (2009), and Pioli et al. (2019) were used and are all reported in terms of the elevation above ground level (agl). The relationship between the maximum plume height in km, H_T , and the mass eruption rate, MER, in g hr^{-1} follows an empirical power law (Aubry et al., 2023; Mastin et al., 2009; Morton et al., 1956; Sparks, 1986; Wilson et al., 1978). The mass eruption rate, MER, also termed the source strength, describes the mass flux per total source area and is commonly derived from H_T when atmospheric dispersion models, such as NAME, are used operationally (Beckett et al., 2024). This is because the plume height is much easier to determine in real-time (e.g., radar, LiDAR measurements, or visual observation) compared to the MER (Dürig et al., 2018; Folch et al., 2012; Pioli & Harris, 2019). In this study, we used the following relationship, based on Aubry et al. (2023), between H_T and MER:

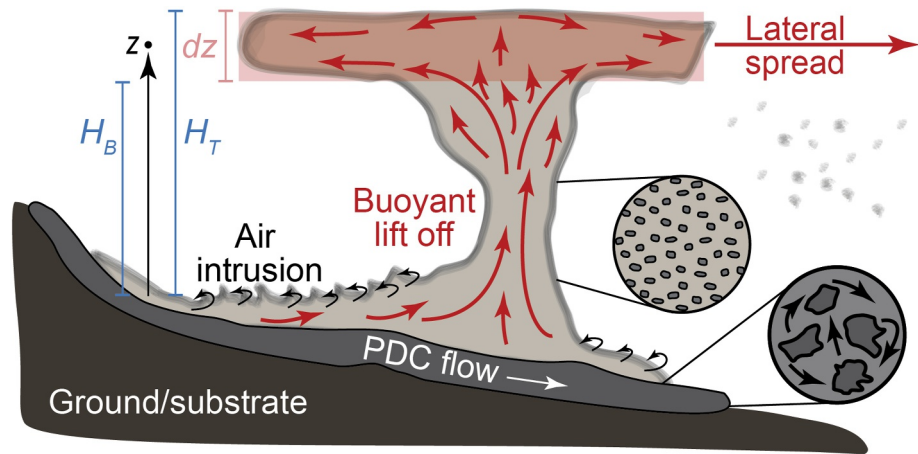


Figure 3. Characteristics of co-PDC plumes. Through air entrainment, parts of the ground-hugging pyroclastic density current become buoyant, and a hot gas-ash mixture lifts off to form a co-PDC plume. The plume reaches a top height, H_T , and spreads laterally at the level of neutral buoyancy where the particles are dispersed over a vertical thickness, dz , (between H_T and H_B ; shaded in red) with a mid-point elevation, z .

$$\text{MER} = \frac{0.226 \sqrt{H_T}}{\sqrt{0.345}} \quad (5)$$

While the relationship of Aubry et al. (2023) has been defined predominantly using information from vent-derived plumes, due to a lack of erupted mass information for co-PDCs, the plume height and mass eruption rate from the MSH co-PDC plume fall within the confidence interval of the fit, and imply that, for at least the largest co-PDC events, this relationship is appropriate.

The ash plume spreads laterally at the neutral buoyancy level, where the density of the plume and the surrounding atmosphere are equal (Carey & Sparks, 1986). This constitutes the umbrella region of the plume and is characterized by a thickness, dz , which corresponds to the height interval of the ash release within the model (Figure 3). The following equation by Carey and Sparks (1986), Morton et al. (1956) and Sparks (1986) describes the relationship between the thickness of the umbrella region and the total column height:

$$dz = H_T - H_B = x \cdot H_T \quad (6)$$

Where H_B is the base of the spreading cloud, and x can take values in the range 0.25–3. Here, we use $x = 0.3$ due to the relationship $H_T = \frac{H_B}{0.7}$ provided by Bonadonna and Phillips (2003). This relationship holds true for all co-PDC plumes under the assumption of no umbrella overshoot.

For our model set up in NAME, we also define the mid-point, z , within the height interval of released ash. The relationships between H_T , H_B , dz , and z are shown visually in Figure 3 and are mathematically expressed as:

$$z = H_T - \frac{1}{2} \cdot dz \quad (7)$$

With substituting Equation 6 into Equation 7, we obtain the final expression for z :

$$z = 0.85 \cdot H_T \quad (8)$$

A full quantitative summary of the parameter ranges is presented in Table 1.

2.4. Particle Characteristics

Ash particles that comprise co-PDCs have been found to have densities between $2,200 \text{ kg m}^{-3}$ and $2,600 \text{ kg m}^{-3}$ (Bonadonna & Phillips, 2003; Watanabe et al., 1999). Given this narrow range and that Beckett et al. (2015)

Table 1
Co-PDC Source Parameters Defined for Historical PDC and Co-PDC Eruptions

Parameter	Symbol	Unit	Min	Max
Area	A	km ²	0.4	619
Aspect ratio	α	–	0.2	1.7
Width of source in plain view	dx	km	0.3	32.4
Length of source in plain view	dy	km	0.5	55.6
Maximal plume height	H_T	km	1	30
Thickness of ash release	dz	km	0.3	9.0

Note. The minimum data (referring to the 1991 eruption of Unzen) for A , α and dx are taken from Watanabe et al. (1999), whereas the maximum data (referring to the 18 May 1980 eruption of Mount St Helens (MSH)) for A , α , and dy are taken from Fisher et al. (1987). We used Unzen and MSH as end-members to describe potential co-PDC plume parameters and behavior. H_T is taken from data sets from Aubry et al. (2021), Eychenne and Engwell (2022), Mastin et al. (2009) and Pioli et al. (2019) and dz from Bonadonna and Phillips (2003) and Carey and Sparks (1986).

showed that differences in particle densities over this range have no significant impact on NAME output, we used 2,500 kg m⁻³ for all our experimental runs. We assumed no aggregation throughout this study.

The total grain size distribution of a co-PDC plume (modified from Marti et al. (2016)) was used for the PSD in NAME and thus specifies the diameter, d , of the particles. The range of particle diameters was split into nine bins with 1.5 φ (phi) intervals between 11.25 φ and -0.75φ , where φ is defined as $\varphi = -\log_2 d(\text{mm})$. The calculated distribution used in this study is shown in Table 2 and all particles were treated as spheres. The mass distribution is further shown in Figure 4.

2.5. Numerical Experiments

We performed two numerical experiments. In the first experiment, we used a constant source strength and plume height but used three different source aspect ratios changing the source area, thus the width and length of the source geometry. Here, we assume that the area and shape of the ground footprint are the same as that at the level of neutral buoyancy where the particles were released. We neglect any plume widening. This allowed us to independently investigate the impact of the source geometric properties on the onward

transport and dispersion of the ash cloud. In the second numerical experiment, we appropriately coupled the plume height, height interval of ash release, and source strength for each run and modeled a range of source geometries and areas. This represents a more realistic set of eruption conditions and allows us to test the influence of MER/ H_T on the simulated location and mass loadings of ash in the downwind cloud.

2.5.1. Numerical Experiment 1: Source Aspect Ratio and Area

This experimental set analyzed the impact of the aspect ratio and total source area on the plume shape and position. The minimum and maximum aspect ratios were determined from the literature as 0.2 and 1.7, respectively and a mid-point value was calculated (0.95) to simply provide a third aspect ratio (cf. Table 1; Figure 2). For each aspect ratio (0.2, 0.95, and 1.7), ten different source areas between 0.4 and 619 km² (Table 1) and the logarithmic mid-point were used. The full model set up conditions that comprise the numerical experiment 1 are displayed in Table 3. All other ESPs were kept constant: H_T was set to 10 km (agl) and thus yielded a dz of 3 km and z , the mid plume height, was 8.5 km. The source strength was set to 1.06×10^{13} g hr⁻¹.

To ensure that any conclusions drawn also hold true for different weather patterns, we perform the same set of numerical experiments for the eight weather patterns defined for the North Atlantic and surrounding European region (Neal et al., 2016). Our study focuses on 31st January 2022, and the meteorology on this day is described by weather pattern 3, where there is negative mean sea level pressure (MSLP) to the west of Iceland and positive MSLP to the southwest, resulting in a (south-)westerly flow. For the results from each of the other weather patterns, the reader is referred to the Supporting Information S1.

2.5.2. Numerical Experiment 2: Coupled H_T and MER for Different A and α

This numerical experiment better represents the natural case, by the appropriate coupling of the plume height H_T , the vertical thickness of ash release dz , and the MER. Specifically, five different plume heights were chosen following Table 1, covering the full range of heights expected for natural co-PDC plumes.

For each plume height, the associated source strength (MER) was calculated using Equation 5 and the thickness of ash release by Equation 6. All other parameters, such as the PSD, the eruption start time (thus meteorological conditions), and the emission duration, were kept constant and are the same as

Table 2
Total Grain Size Distribution (TGSD) Modified From Marti et al. (2016)

d (φ -scale)	d (μm)	Cumulative volume
11.25	0.41	0
9.75	1.16	0.0051
8.25	3.28	0.0415
6.75	9.29	0.1799
5.25	26.28	0.4882
3.75	74.33	0.8027
2.25	210.22	0.9433
0.75	594.60	0.9864
-0.75	1681.79	1

Note. The particle diameters, d , were grouped into equal bins with 1.5 φ intervals.

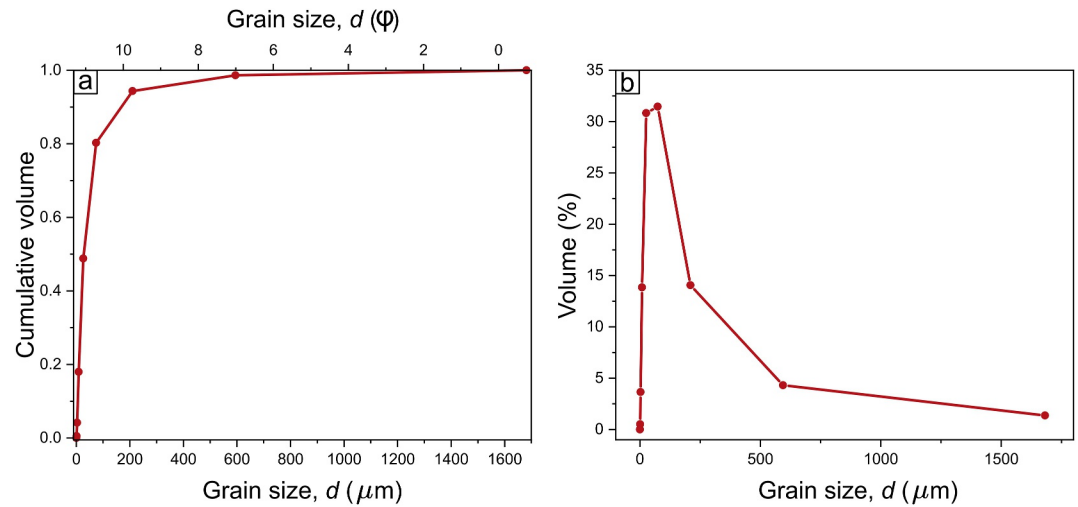


Figure 4. The total grain size distribution (modified) from Marti et al. (2016) for (a) cumulative volume distribution and (b) particle size fraction.

in experiment 1. These different cases have all been modeled by using two different aspect ratios and the minimum, middle, and maximum source geometry areas, with both wet and dry deposition included. Table 4 provides the full model set-up conditions of numerical experiment 2, indicating the plume height dz , MER, α , A , dx , dy , and the run number for each model run.

3. Results and Discussion

In this section, we will show the results from our systematic NAME model runs (as outlined in Tables 3 and 4) and consider the individual impact of different source parameters on the transport and dispersion of the co-PDC ash cloud. To do this, and to provide a common comparison across all runs, we use the horizontal position and extent

Table 3
Source Parameters of Numerical Experiment 1

Run: $\alpha = 0.2$	(1)	(2)	(3)	(4)	(5)	(6)	(7)	(8)	(9)	(10)	(11)
A (km^2)	0.4	1	2	5	10	16	24	50	121	274	619
dx (km)	0.3	0.4	0.6	1.0	1.4	1.8	2.2	3.2	4.9	7.4	11.1
dy (km)	1.4	2.1	3.2	4.8	7.2	8.9	10.9	15.9	24.6	37.0	55.6
P (km)	3.4	5.0	7.6	11.6	17.2	21.4	26.2	38.2	59.0	88.8	133.4
Run: $\alpha = 1.7$	(12)	(13)	(14)	(15)	(16)	(17)	(18)	(19)	(20)	(21)	(22)
A (km^2)	0.4	1	2	5	10	16	24	50	121	274	619
dx (km)	0.8	1.2	1.9	2.8	4.2	5.2	6.3	9.3	14.3	21.6	32.4
dy (km)	0.5	0.7	1.1	1.6	2.5	3.1	3.7	5.4	8.4	12.7	19.1
P (km)	2.6	3.8	6.0	8.8	13.4	16.6	20.0	29.4	45.4	68.6	103.0
Run: $\alpha = 0.95$	(23)	(24)	(25)	(26)	(27)	(28)	(29)	(30)	(31)	(32)	(33)
A (km^2)	0.4	1	2	5	10	16	24	50	121	274	619
dx (km)	0.6	0.9	1.4	2.1	3.2	3.9	4.7	6.9	10.7	16.1	24.2
dy (km)	0.6	1.0	1.5	2.2	3.3	4.1	5.0	7.3	11.3	17.0	25.5
P (km)	2.4	3.8	5.8	8.6	13.0	16.0	19.4	28.4	44.0	66.2	99.4

Note. Three different aspect ratios were each used for 11 different source geometry areas. The width and length of the geometry were determined by Equations 3 and 4. Runs (1) to (11) used an aspect ratio of 0.2, runs (12) to (22) used an aspect ratio of 1.7, and runs (23) to (33) used the mid aspect ratio of 0.95. The source perimeter, $P = 2 \cdot dx + 2 \cdot dy$, is also indicated for comparison.

Table 4
Source Parameters for Numerical Experiment 2

H_T (km)	z (km)	dz (km)	MER	α				
1	0.85	0.3	1.41E + 02 (kg s ⁻¹) = 5.07E + 08 (g hr ⁻¹)	0.2	Run	(1)	(2)	(3)
					A (km ²)	0.4	16	619
					dx (km)	0.3	1.8	11.1
					dy (km)	1.4	8.9	55.6
					P (km)	3.4	12.5	133.4
				1.7	Run	(4)	(5)	(6)
					A (km ²)	0.4	16	619
					dx (km)	0.8	5.2	32.4
					dy (km)	0.5	3.1	19.1
					P (km)	2.6	16.6	103.0
5	4.25	1.5	1.12E + 05 (kg s ⁻¹) = 4.03E + 11 (g hr ⁻¹)	0.2	Run	(7)	(8)	(9)
					A (km ²)	0.4	16	619
					dx (km)	0.3	1.8	11.1
					dy (km)	1.4	8.9	55.6
					P (km)	3.4	12.5	133.4
				1.7	Run	(10)	(11)	(12)
					A (km ²)	0.4	16	619
					dx (km)	0.8	5.2	32.4
					dy (km)	0.5	3.1	19.1
					P (km)	2.6	16.6	103.0
10	8.5	3.0	1.99E + 06 (kg s ⁻¹) = 7.15E + 12 (g hr ⁻¹)	0.2	Run	(13)	(14)	(15)
					A (km ²)	0.4	16	619
					dx (km)	0.3	1.8	11.1
					dy (km)	1.4	8.9	55.6
					P (km)	3.4	12.5	133.4
				1.7	Run	(16)	(17)	(18)
					A (km ²)	0.4	16	619
					dx (km)	0.8	5.2	32.4
					dy (km)	0.5	3.1	19.1
					P (km)	2.6	16.6	103.0
20	17.0	6.0	3.53E + 07 (kg s ⁻¹) = 1.27E + 14 (g hr ⁻¹)	0.2	Run	(19)	(20)	(21)
					A (km ²)	0.4	16	619
					dx (km)	0.3	1.8	11.1
					dy (km)	1.4	8.9	55.6
					P (km)	3.4	12.5	133.4
				1.7	Run	(22)	(23)	(24)
					A (km ²)	0.4	16	619
					dx (km)	0.8	5.2	32.4
					dy (km)	0.5	3.1	19.1
					P (km)	2.6	16.6	103.0
27	22.95	8.1	1.22E + 08 (kg s ⁻¹) = 4.41E + 14 (g hr ⁻¹)	0.2	Run	(25)	(26)	(27)
					A (km ²)	0.4	16	619
					dx (km)	0.3	1.8	11.1
					dy (km)	1.4	8.9	55.6
					P (km)	3.4	12.5	133.4

Table 4
Continued

	1.7	Run	(28)	(29)	(30)
A (km ²)			0.4	16	619
dx (km)			0.8	5.2	32.4
dy (km)			0.5	3.1	19.1
P (km)			2.6	16.6	103.0

Note. Different total plume heights define the thickness of ash release and source strength (MER), which were tested for different source geometries (aspect ratios and areas). The designated reference number of each model run is given in brackets and highlighted in gray. The source perimeter, $P = 2 \cdot dx + 2 \cdot dy$, is also indicated for comparison.

of the whole ash cloud and the total column mass loading. The total column mass loading is the sum of all ash vertically above the ground at a given location and thus has units of g m^{-2} . These data are extracted every hour after the emission/eruption started (t_0) up until 24 hr later. We applied a threshold of 0.2 g m^{-2} as it aligns to the threshold which satellite instruments can typically detect and retrieve volcanic ash (Saint et al., 2024). Furthermore, it is the lowest concentration threshold required for VAAC forecasts, if we assume the ash cloud has a 1 km thickness (Beckett et al., 2020).

3.1. Impact of Source Area, A

First, let us consider the impact of the source area, A , for a constant source aspect ratio, α . Figure 5 provides an overview of the size and orientation of all source geometries used in this study. They are shown in their true

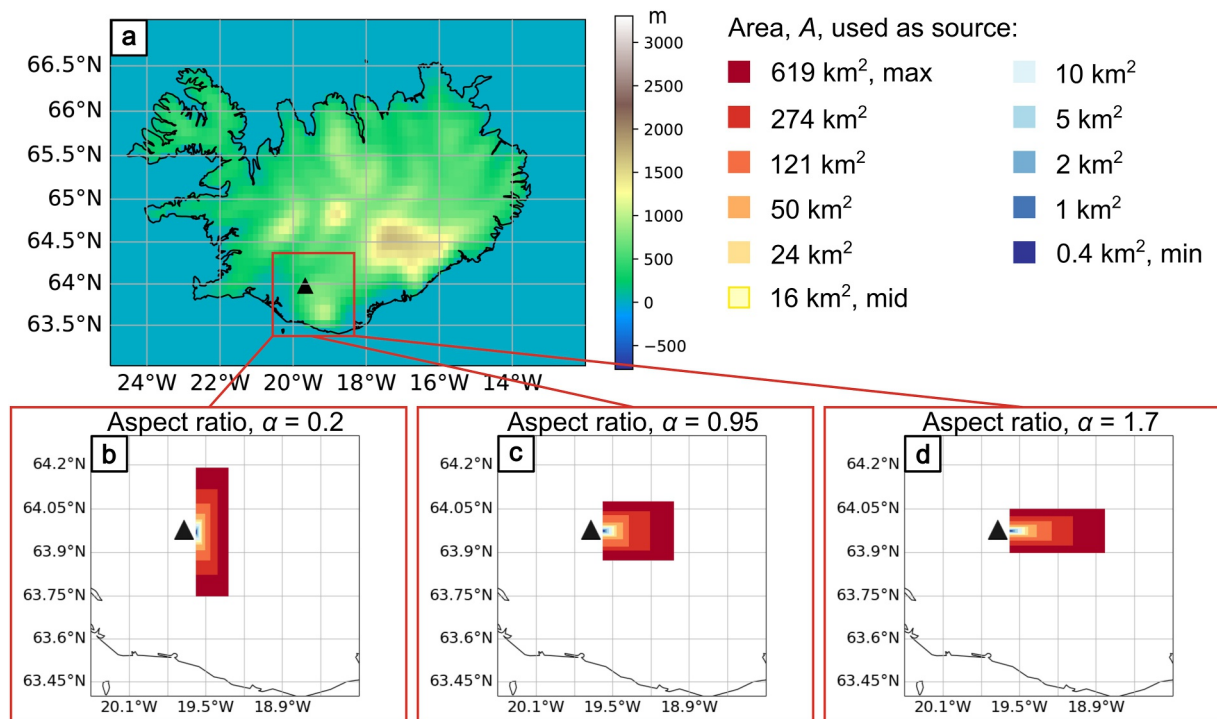


Figure 5. Orientation and size of the source for the different aspect ratios and areas used in our model runs. (a) Map of Iceland, showing the ground elevation using the global 10 km resolution topography data used with the NAME simulations. The color bar shows the ground elevation in meters above sea level. The lower panels show the range of source areas for aspect ratios, (b) $\alpha_{\min} = 0.2$, (c) $\alpha_{\text{mid}} = 0.95$, and (d) $\alpha_{\max} = 1.7$ used in this study.

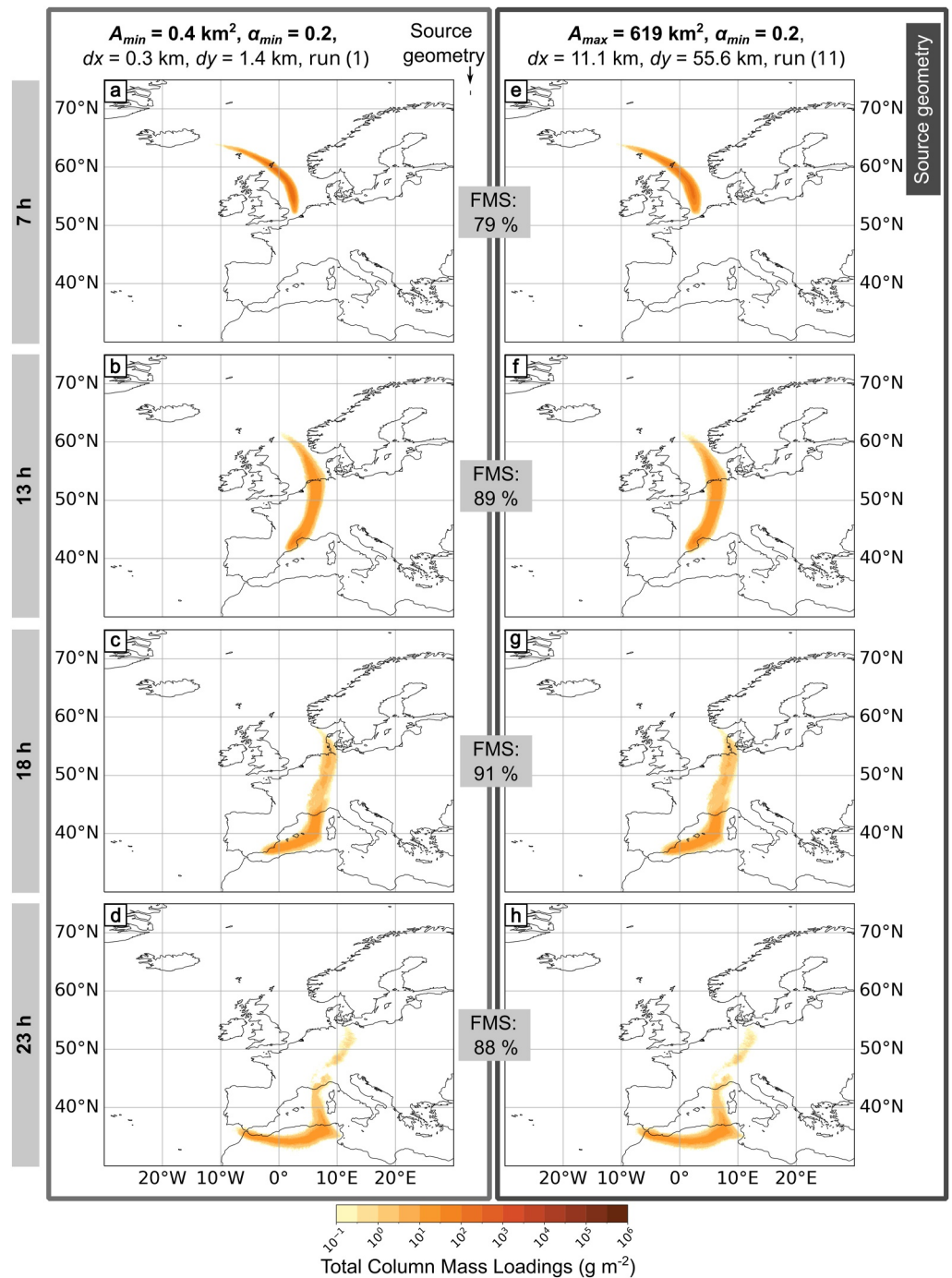


Figure 6. NAME outputs for numerical experiment 1, all using $\alpha_{\min} = 0.2$, a 1 hr particle release, $z = 8.5$ km, $dz = 3$ km and $MER = 1.06 \times 10^{13}$ g hr $^{-1}$. The panels on the left are for the minimum source area, and the panels on the right are for the maximum. The area and orientation of the two source geometries are compared in relation to each other next to the parameter list at the top of the figure. For each area, four outputs are presented at different times after the eruption start t_0 : (a and e) 7 hr, (b and f) 13 hr, (c and g) 18 hr, and (d and h) 23 hr. Total column mass loadings are averaged over the previous hour, and we applied a threshold of 0.2 g m $^{-2}$.

locations with respect to Hekla volcano (black triangle) and Iceland. For context, Iceland has a total land area of approximately $104,000$ km 2 and the minimum and maximum co-PDC plume source areas were 0.4 and 619 km 2 , respectively.

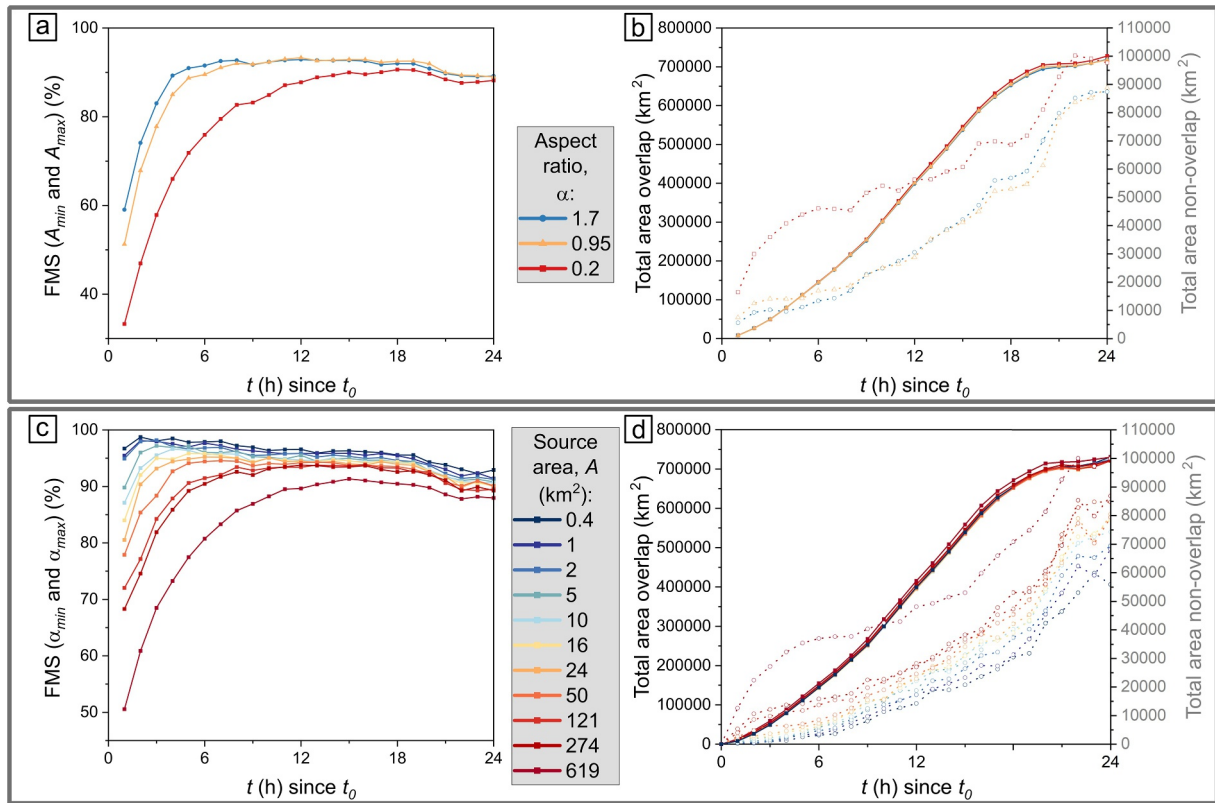


Figure 7. Figure of Merit in space (FMS) and total cloud area overlap within numerical experiment 1. (a) FMS between the plumes generated using minimum (A_{min}) and maximum (A_{max}) source areas. The different colored data points correspond to different aspect ratios. (b) Actual area overlap between A_{min} and A_{max} . All lines almost overlap. The total non-overlapping area is given in dotted lines, with a gray-colored y-axis on the right-hand side. (c) FMS between the plumes generated with the minimum (α_{min}) and maximum (α_{max}) aspect ratio. The different colored data points correspond to different source areas. (d) Actual area of overlap between α_{min} and α_{max} . All lines almost overlap. The total non-overlapping area is given in dotted lines, with a gray-colored y-axis on the right-hand side. The lines between data points are not model fits and are just used to guide the eye.

To compare the ash cloud generated by different source geometry areas, we plotted the ash clouds from a 0.4 km² (min) and 619 km² (max) source area, both with aspect ratio, $\alpha_{min} = 0.2$. These results are shown in Figure 6. The simulated ash clouds grow with time, following the wind field toward the east and show similar downwind shapes. The initial latitudinal extent of the ash clouds close to the source location shows the most deviation; however, as the age of the cloud increases and it becomes more dispersed, the differences between the simulations initialized with minimum and maximum source areas are insignificant. Quantitatively, the difference in cloud position was compared between these two end-member cases using the Figure of Merit in Space (FMS) (Rolph et al., 2014; Warner et al., 2004):

$$FMS = \frac{A_1 \cap A_2}{A_1 \cup A_2} \cdot 100 \quad (9)$$

where A_1 is the cloud area within one model output and A_2 the cloud area in another model output. The intersection is compared with the union of these areas. The areas correspond to the forecasted cloud areas with mass loading $\geq 0.2 \text{ g m}^{-2}$. High FMS values correspond to high agreement between the models. These results are shown in Figure 7a.

For all aspect ratios, the FMS calculated between the ash clouds generated by model runs using the minimum (A_{min}) and maximum (A_{max}) source areas increases with time after t_0 until a plateau is reached. The near-source variations are more pronounced as there is less cloud area to compare with. The plateau occurs at $\sim 90\%$ FMS for all aspect ratios, but is achieved faster for the larger aspect ratios (Figure 7a). Additionally, in all cases, there is a slight decrease in the FMS after ~ 20 hr. We also find that generally $\alpha_{min} = 0.2$ has the lowest FMS values.

However, the actual overlapping cloud area is still the largest for $\alpha_{\min} = 0.2$ with values up to 728,000 km² (Figure 7b). It must be stressed that this is not strictly related to the value of the aspect ratio but to the applied weather conditions. This can be visualized in Figure 5 as the larger areas with $\alpha = 0.2$ show a larger longitudinal extension. The extension in source geometry is perpendicular to the wind direction, and thus, there is more variability in the particle trajectories (especially in the first few hours since t_0). If the source geometry is elongated with its long axis in the dominant wind direction (i.e., the larger of dx or dy is parallel to the wind direction), there is a lower impact on differences in particle trajectories. The area of non-overlap, added for completeness, also increases with time (Figure 7b).

The differences can also be evaluated in terms of total column mass loadings. For all cases, higher total column mass loadings are found closer to the source location and at times closer to the start of the release (e.g., Figure 6). Between the model runs with different source areas, small changes in total column mass loadings toward the tip of the ash cloud are noticeable. However, these are only identified within the first ~7 hr, and at later times, differences become indistinguishable. In general, even when the source area is changed by three orders of magnitude, only small differences in downwind cloud shape and column mass loading are observed. This is true for the full range of aspect ratios tested and the supporting plots for $\alpha = 0.95$ and $\alpha = 1.7$ are shown in Figures S2 and S3 in Supporting Information S1.

3.2. Impact of the Aspect Ratio of the Source, α

To evaluate the impact of changing the aspect ratio of the source, α , we present the results from model runs for α_{\min} and α_{\max} at a common source area. The definition of the aspect ratio (Equation 1) as the ratio between dx and dy was chosen here to quantitatively describe the relationship between the width and the length of the source area. However, this enables aspect ratios to range from almost zero to infinity. Other definitions of the source geometry are possible, such as taking the ratio between the minimum and maximum dimensions, thus quantifying how equant the source area is.

Simulated total column mass loadings are shown in Figure 8 for $A_{\max} = 619$ km². There are only very small differences in the shape of the modeled cloud. After 7 hr since t_0 , the tip of the ash cloud appears thinner for $\alpha_{\max} = 1.7$ (Figure 8e), compared to $\alpha_{\min} = 0.2$ (Figure 8a). The FMS of the cloud area ranges from 83% to 90%. We consider these differences to be small given the order of magnitude change in the source aspect ratio (0.2 vs. 1.7). Similar results are shown when comparing α_{\min} and α_{\max} for $A_{\min} = 0.4$ km² and the related plots are shown in Figure S4 in Supporting Information S1. Here, the FMS in the cloud areas is greater, and ranges from 98% to 92% from 7 to 23 hr since t_0 , and thus slightly decreases with time during this 7–23 hr period. Figure 7c compares the FMS of the ash cloud area between the minimum (α_{\min}) and maximum (α_{\max}) aspect ratios. In general, greater FMS values correspond to model runs with smaller source areas, whereas the actual area overlap is almost the same for all source areas and increases with time as well as the area of non-overlap (Figure 7d). Small source areas ($A < 5$ km²) have large FMS (>95%) until 4 hr after t_0 , which slowly decreases with increased time after. However, at 24 hr since t_0 , the FMS is still >90%. For the other source areas, $A \geq 5$ km², the FMS increases until (at least) 8 hr, plateaus around 90% and then slightly decreases. The largest source area tested, $A = 619$ km², has the lowest FMS overall and is 51% at 1 hr since t_0 and 88% at 24 hr since t_0 (Figure 7c).

3.3. Evaluation of Geometric Source Properties (A and α) on Co-PDC Ash Transport and Dispersion

We now synthesize the results of the previous sections, that compared the impact of source area and aspect ratio, respectively. To supplement the visual comparisons between the NAME model outputs (cf. Figures 6 and 8), we introduce the use of the relative standard deviation, %RSD:

$$\%RSD = \frac{\sigma}{\bar{x}} \cdot 100 \quad (10)$$

where σ is the standard deviation of the data set under study (e.g., cloud area at each hour after eruption start for all cloud areas) and \bar{x} is the average of the data set (i.e., the ash cloud area generated throughout experiment 1 per given modeled time).

To compare different forecasts, we use the FMS, which is a measure of accuracy that has often been used for volcanic ash cloud forecasts (Rolph et al., 2014; Wilkins et al., 2016), as well as the %RSD of the cloud area for a

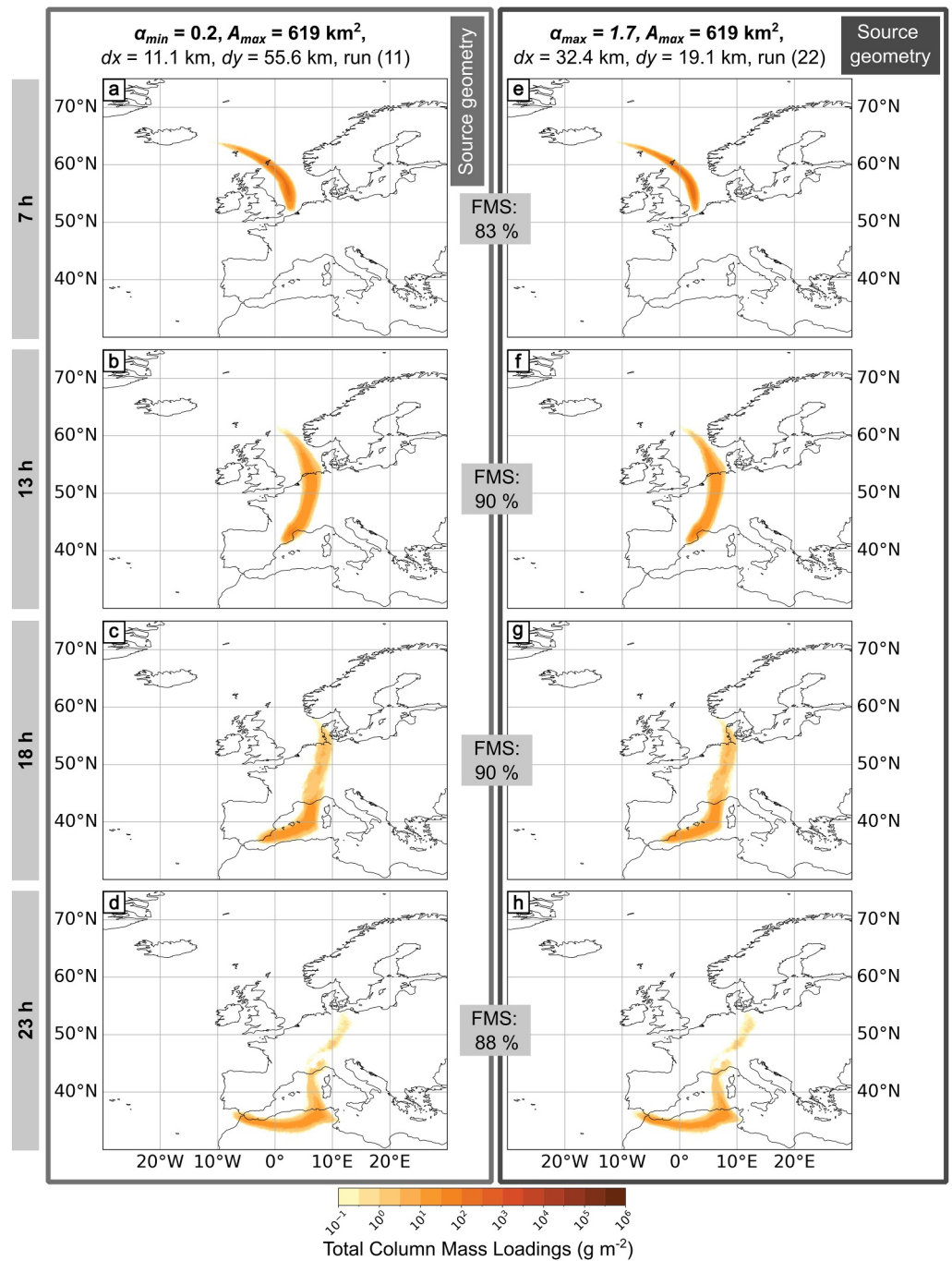


Figure 8. NAME model outputs for numerical experiment 1, all using $A_{max} = 619 \text{ km}^2$, a 1 hr particle release, $z = 8.5 \text{ km}$, $dz = 3 \text{ km}$ and $MER = 1.06 \times 10^{13} \text{ g hr}^{-1}$. The left figure panels (a–d) show results from the minimum aspect ratio $\alpha_{min} = 0.2$, and the right panels (e–h) show the maximum aspect ratio $\alpha_{max} = 1.7$. The area and orientation of the two source geometries are compared in relation to each other next to the parameter list at the top of the figure. For each aspect ratio, four outputs at different times after eruption start t_0 are shown: (a and e) 7 hr, (b and f) 13 hr, (c and g) 18 hr and (d and h) 23 hr. Total column mass loadings are averaged over the previous hour, and we applied a threshold of 0.2 g m^{-2} .

group of forecasts. The FMS provides a simple score of how well the clouds from the different forecasts overlap and here we consider a score of $\geq 75\%$ to very good. The %RSD provides a measure of the spread in the total area provided by a group of forecasts without regard to how well they overlap. Here, we consider that the differences in total areas provided by a group of forecasts are insignificant when %RSD falls below 10%. To complement these

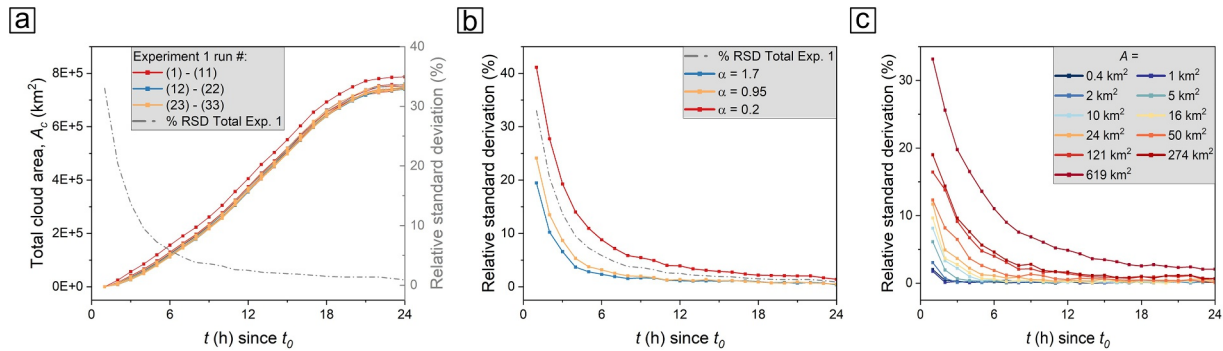


Figure 9. Total cloud area, A_c , for numerical experiment 1. (a) The total cloud area, A_c , for all model runs across Experiment 1. Although all lines (1) to (33) are represented, they mostly overlap. The %RSD is indicated by the gray dotted line. (b) Experiment 1 separated per aspect ratio, taking all source areas into account. $\alpha_{\min} = 0.2$ has a larger %RSD, as the longitudinal distance becomes more important with the specific applied weather conditions. There is no linear relationship between %RSD and α . (c) Experiment 1 separated per source area A , where one line represents three runs each ($\alpha_{\min} = 0.2$, $\alpha_{\text{mid}} = 0.95$ and $\alpha_{\text{max}} = 1.7$). The larger the source area, the larger the %RSD. In all panels, the lines between data points are not model fits and are just used to guide the eye.

measures, we also provide some discussion of the total area of overlap and non-overlap among some of the forecasts.

Due to the ~ 10 km horizontal resolution of the meteorological data used with our NAME simulations, source areas approximately $A \geq 10$ km² can have, in at least one dimension, a source geometry that is larger than the grid resolution and therefore crosses multiple meteorological grid cells. However, despite this, the total ash mass in the atmosphere is remarkably similar for all runs in experiment 1 and the data almost overlap (Figure S5 in Supporting Information S1). The total mass in the atmosphere has been studied for both the total data set and with the threshold of 0.2 g m⁻² applied. There are only minor differences between these data sets when the threshold is applied. The total mass in the atmosphere reaches a maximum after 1 hr (the total time of particle emission) and then decays as ash is removed through wet and dry deposition (including sedimentation). Across all model outputs of experiment 1, differences in total mass are less than 0.4%; thus, we can say that the total mass in the atmosphere is not affected by changing the source aspect ratio or source area.

Overall, like the total mass in the atmosphere, the total cloud area, A_c , shows minor variation across all the source areas and aspect ratios investigated (Figure 9). The only exception is at times close to the start of particle emission, t_0 and thus at cloud locations close to the source. Comparing all runs in experiment 1 (gray dotted line in Figures 9a and 9b) close to the start time (1 hr since t_0), the relative standard deviation is 33%. However, these high %RSD values rapidly reduce to 9.5% after 4 hr since t_0 and reach a low plateau of $\sim 2\%$ after 13 hr. Furthermore, the total cloud area increases and shows little deviation between the different applied aspect ratios (Figure 9a). By further analyzing the cloud area, A_c , for a set plume height (here, $H_T = 10$ km), the influence of aspect ratio (Figure 9b) and area of the source geometry (Figure 9c) can be quantitatively investigated. First, comparing different aspect ratios $\alpha_{\min} = 0.2$ has a maximum %RSD of 41% and reduces to $<10\%$ after 6 hr, whereas $\alpha_{\text{mid}} = 0.95$ shows a maximum %RSD of 24% and becomes insignificant ($\leq 9\%$) after 3 hr, and $\alpha = 1.7$ shows a maximum %RSD of 19% and becomes insignificant ($\leq 6.5\%$) after 3 hr.

Furthermore, comparing the different source areas (each averaged over all three aspect ratios) used in experiment 1 (Figure 9c), we find that the larger the source area, the higher the %RSD. The %RSD decays with time for all source areas. $A_{\text{max}} = 619$ km² shows the largest %RSD of 33% at 1 hr after particle release, whereas $A = 1$ km² shows only 1.8% RSD at the same time. Additionally, for a given time t , the %RSD is lower for smaller source areas. Only $A_{\min} = 0.4$ km² and $A = 1$ km² do not exactly follow this observation until reaching 5 hr since t_0 ; however, the %RSD is always $\leq 2\%$. For all source areas at 6 hr after particle release, the %RSD is $<10\%$.

Our observations that the cloud area growth is little impacted by the source geometry and aspect ratio can be explained mathematically. The cloud area can be described as

$$A(t) = A_0 + \int_0^t \left(\oint_{\partial A(\tau)} v_n(x, \tau) ds \right) d\tau \quad (11)$$

where A_0 is the source area at origin, $\partial A(\tau)$ is the boundary of the cloud at time τ , and $v_n(x, \tau)$ is the normal expansion rate at point x on the boundary. The derivative, describing the rate of change of the area,

$$\frac{dA(t)}{dt} = \oint_{\partial A(t)} v_n(x, t) ds \quad (12)$$

can be studied under the assumption of a rectangular source geometry with width l_{x0} and length l_{y0} expanding at constant rates v_x and v_y (uniform wind field). The area as a function of time, therefore, describes

$$A(t) = l_{x0}l_{y0} + t(v_x l_{y0} + v_y l_{x0}) + v_x v_y t^2 \quad (13)$$

The quadratic term $v_x v_y t^2$, being of leading order at $t \gg 0$, is not impacted by the initial source geometry at the source location. This therefore explains both the decrease in the %RSD (Figure 9) and the convergence in total cloud area between all the runs with time as shown by the FMS (Figure 7). For $t \sim 0$ hr and times close to the eruption start, the ash cloud expands dominantly in the wind direction (v_x for our specific date here). Therefore, the extent of the perpendicular dimension, with respect to the wind (l_{y0} here) is of greater influence than the parallel dimension (l_{x0} here). The linear term $l_{x0}l_{y0}$ is proportional to the perimeter (of the rectangular shape) and this therefore explains the high relative standard deviation between different aspect ratios.

For typical vent-derived plumes, Mastin and Van Eaton (2020) have shown that considering the associated umbrella cloud growth is crucial for accurate modeling of the ash cloud area and downwind extent. They also show, as in this study, that the difference between cloud areas decreases with time after eruption. However, umbrella cloud areas typically range between 50 km² and 1,600,000 km² (Constantinescu et al., 2021; Mastin & Van Eaton, 2020; Prata et al., 2025; Zidikheri et al., 2017) and thus are larger than typical co-PDC clouds (e. g., 0.4–619 km²). This further supports our observations that co-PDC cloud transport and dispersal (across the range of meteorological conditions tested here) is not impacted by the source area (due to the smaller contribution of the linear term in Equation 13).

3.4. The Impact of Co-PDC Plume H_T and MER

The modeled ash cloud shows completely different transport and dispersion patterns when changing H_T , and thus MER and dz . To illustrate this, in Figure 10 we show NAME outputs at 12 hr (left side of figure) and 23 hr since t_0 (right side of figure) initialized using a range of plume heights (H_T) for $A_{\max} = 619$ km² with $\alpha_{\min} = 0.2$. In general, modeled total column mass loadings increase with H_T and the larger H_T and MER are, the larger the ash cloud becomes. For $H_T = 1$ km (Figures 10a and 10f), the total column mass loading threshold of 0.2 g m⁻² was not reached. The cloud generated by $H_T = 5$ km has mass loadings ≥ 0.2 g m⁻² at 12 hr (Figure 10b) and 23 hr since t_0 (Figure 10g) but beyond 23 hr, mass loadings are relatively low. The ash clouds generated by $H_T = 20$ km (Figure 10d) and $H_T = 27$ km (Figure 10e) form a relatively compact area at 12 hr after particle release; however, they become more elongated and stretched over wider areas for 23 hr (Figures 10i and 10j). For consistency, a set of model runs using $A_{\max} = 619$ km² with $\alpha_{\max} = 1.7$ and $A_{\min} = 0.4$ km² with $\alpha_{\min} = 0.2$ and $\alpha_{\max} = 1.7$ are shown in Figures S6 to S8 in Supporting Information S1. These combinations bracket the extremes in natural parameter space and still follow the general relationships described here. As shown in Figure 11, all ash cloud areas increase with time after the beginning of particle emission (t_0) and larger initial plume heights (H_T), thus larger mass eruption rates, correspond to larger cloud areas.

Figure 12 shows the total modeled mass in the atmosphere with time. As expected, with increasing plume height (and thus MER), the total mass in the atmosphere (and the total column mass loadings in Figure 10) also increases. The maximum total mass occurs (for each plume height) after 1 hr, which is the end of the emission time. The total mass in the atmosphere released from higher plumes ($H_T = 10$ km, $H_T = 20$ km and $H_T = 27$ km) remains almost constant, slightly decreasing, while when $H_T = 1$ km and $H_T = 5$ km, there is a larger reduction/decay with time. When $H_T = 1$ km, the total mass decreases to 0.004% of the initial total mass at 24 hr since t_0 , whereas when $H_T = 27$ km, the ash cloud retains 68% of its initial total mass after 24 hr.

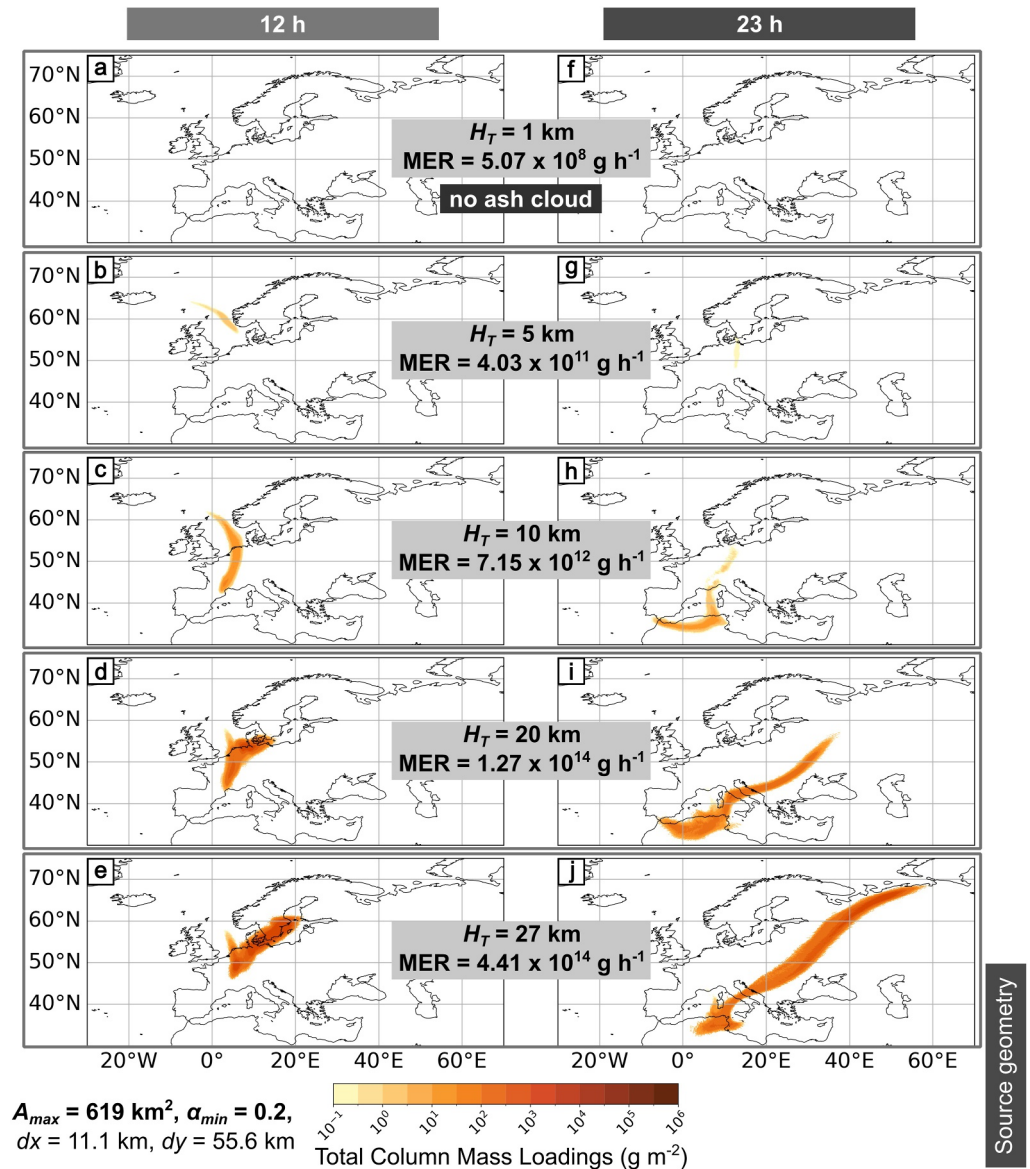


Figure 10. NAME model outputs for numerical experiment 2, all using a 1 hr particle release with different H_T , MER, and dz . The figure panels on the left (a–d) are for 12 hr after eruption start t_0 , and the panels on the right (e–h) show 23 hr after eruption start t_0 . The outputs here are for $A_{\max} = 619 \text{ km}^2$ with $\alpha_{\min} = 0.2$. With increasing H_T and $t_0 + t$ (hr), the plume size grows. Total column mass loadings are averaged over the previous hour, and we applied a threshold of 0.2 g m^{-2} . The subplots (a and f) show no ash cloud (i.e., mass loading $< 0.2 \text{ g m}^{-2}$).

3.5. Outlook and Future Work

NAME models the long-range transport and dispersion of ash clouds. In this study, we have represented the release of ash into the atmosphere with a set of ESPs. However, additional schemes can be coupled to NAME to represent vent proximal behavior, including those for buoyant plumes and umbrella clouds (Beckett et al., 2015; Devenish, 2013; Webster et al., 2012, 2020). At the expense of increased computational time, these schemes could be applied to investigate the dynamics of co-PDCs and, when coupled to NAME, their impact on the long-range transport of the resulting ash cloud.

We have assumed an emission duration of 1 hr. This aligns with the resolution of the averaging period used for the modeled total column mass loadings. It is expected that co-PDC plumes will have a range of ash emission times corresponding to eruption parameters such as the MER and source area; however, no quantitative relationships

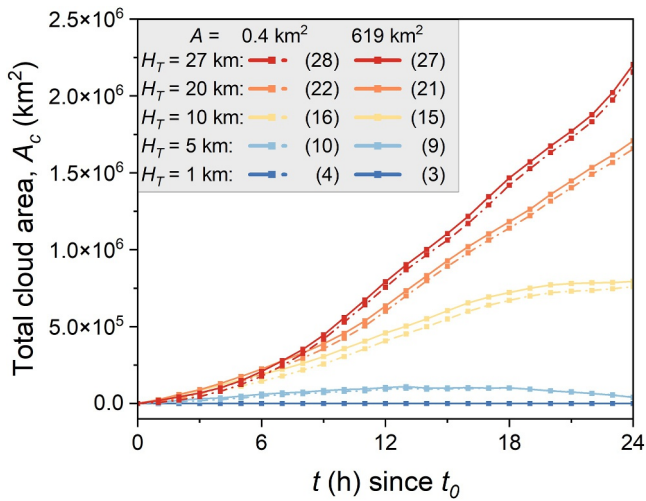


Figure 11. The total cloud area as a function of time for model runs within numerical experiment 2. The five different colors correspond to the different plume heights. Each with $A_{\min} = 0.4 \text{ km}^2$ for $\alpha_{\max} = 1.7$ and $A_{\max} = 619 \text{ km}^2$ for $\alpha_{\min} = 0.2$ as a dotted and solid line, respectively. The total plume area, A_c , increases for all plume heights with time within the first 13 hr. $H_T = 1 \text{ km}$ and $H_T = 5 \text{ km}$ decay afterward, while the others continue to increase. The numbers in brackets correspond to the model run number. The lines between data points are not model fits and are just used to guide the eye.

which has a horizontal resolution of $\sim 10 \text{ km}$, which has been shown to be optimal for representing long-range transport of ash clouds (see Beckett et al., 2020). We have repeated numerical experiment 1 for eight different weather patterns (Neal et al., 2016), which represent the variation in circulation types expected for this region (Figures S18 to S66 in Supporting Information S1). The exact cloud shape and location vary with different weather patterns and dates, but we show that the impact of source area and aspect ratio is negligible across the data set.

Here, we have used NWP data from the Global configuration of the UM, which has a horizontal resolution of $\sim 10 \text{ km}$, which has been shown to be optimal for representing long-range transport of ash clouds (see Beckett et al., 2020). We have repeated numerical experiment 1 for eight different weather patterns (Neal et al., 2016), which represent the variation in circulation types expected for this region (Figures S18 to S66 in Supporting Information S1). The exact cloud shape and location vary with different weather patterns and dates, but we show that the impact of source area and aspect ratio is negligible across the data set. The FMS plateaus $\geq 75\%$ for all source areas, aspect ratios and weather patterns (Figures S19, S26, S33, S40, S47, S54, and S61 in Supporting Information S1). However, further investigation is needed to determine if there is any impact with different seasons or climates or any specific meteorological conditions, for example, sea breezes.

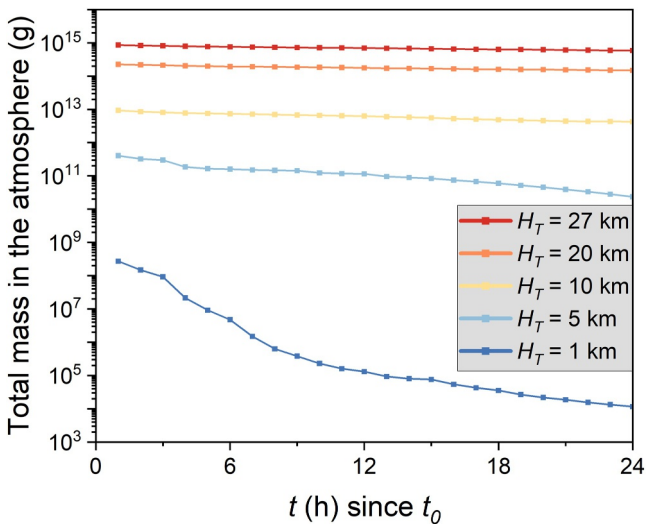


Figure 12. Total mass in atmosphere per plume height in numerical experiment 2. For visual clarity, only $A_{\max} = 619 \text{ km}^2$, $\alpha_{\min} = 0.2$ are shown here, but the other runs show a similar relationship. For all plume heights, the total mass in the atmosphere is greatest at 1 hr since t_0 (end of particle emission) and decays afterward. The smaller the plume height, the greater the decay. The lines between data points are not model fits and are just used to guide the eye.

Modeled total column mass loadings were not found to be sensitive to the source area and aspect ratio. However, further work should also consider the impact on the vertical distribution of ash in the atmosphere and predicted ash concentrations (mg m^{-3}), aligned to the requirements for VAACs to provide quantitative forecasts.

The applied relationship between H_T and MER is well established for point sources; however, it is not clear how well this applies for elongated source geometries. Unknown, so far, is how the source area and MER are impacted by entrainment of ambient air, changing the particle concentration across the plume for these elongated source geometries. We assume entrainment to be lower along the edges of a linear plume than along the edges of a circular plume. It remains to be investigated whether large areas, $A_{\max} = 619 \text{ km}^2$, are still likely to reach a plume height of $H_T = 30 \text{ km}$ with the same MER predicted by the power law relationship derived from vent-derived plume information (Aubry et al., 2023) and whether the assumption of a uniform MER over the whole source area is suitable. Although the co-PDC plume of MSH falls within the confidence interval of the MER relationship used here, smaller co-PDC plumes might be better described by a different plume scheme, for example, a thermal buoyant plume, with an instantaneous mass release,

meaning that the MER- H_T relationship might be different (Biass et al., 2016; Bonadonna, Macedonio, et al., 2002; Druitt et al., 2002; Woods & Kienle, 1994).

The use of inversion approaches, such as that outlined by Pelley et al. (2021) to optimally constrain the time-varying distribution of mass with height at the source for vent-derived plumes, has proved to be powerful tools during operational response when information may be scarce. Given our results show that capturing the plume height and MER is fundamentally important for co-PDC plumes too, the use of inversion tools for this type of event will also be beneficial. Some inversion approaches have also explored optimizing the source geometry for umbrella cloud releases (Zidikheri et al., 2017). Here we have shown that after the first few hours, this is not a key parameter (due to its relatively small source area compared to umbrella clouds), however such an approach could also be further explored.

4. Conclusion

We studied the transport and dispersion of a volcanic ash cloud generated from a co-PDC plume to assess the sensitivity to the ESPs used to initialize model simulations. Co-PDC ash plumes/clouds, generated from PDCs, have unique source properties, in particular their PSD and source geometry are different from typical eruption plumes. Our sensitivity study showed that changes in the source area and the aspect ratio of the source have only a minor impact on the resultant cloud location and its total column mass loadings after ~6 hr from the start of the release. The impact is greatest if the long axis of the source geometry is perpendicular to the wind direction. However, as previously established for vent-derived plumes, the plume height and corresponding mass eruption rate are leading order parameters. Here, we have shown that they yield significant differences when modeling the transport and dispersion of co-PDC ash clouds. This result suggests that VAACs may not need to obtain a detailed description of the co-PDC source geometry, which would be difficult to establish quickly, and rather the operational response should continue to focus on assigning optimal plume heights and MERs.

Conflict of Interest

The authors declare no conflicts of interest relevant to this study.

Availability Statement

NAME III Version 8.5 was used in the transport and dispersion model simulations. The UK Met Office NAME model and UM output to drive NAME are available via license from the UK Met Office (© Crown Copyright, Met Office): <https://www.metoffice.gov.uk/research/approach/modelling-systems/dispersion-model>. The script used to generate the data in this contribution can be found on Zenodo (Hagenbourger et al., 2025).

References

- Andrews, B. J., & Manga, M. (2011). Effects of topography on pyroclastic density current runout and formation of coignimbrites. *Geology*, 39(12), 1099–1102. <https://doi.org/10.1130/G32226.1>
- Andrews, B. J., & Manga, M. (2012). Experimental study of turbulence, sedimentation, and coignimbrite mass partitioning in dilute pyroclastic density currents. *Journal of Volcanology and Geothermal Research*, 225–226, 30–44. <https://doi.org/10.1016/j.jvolgeores.2012.02.011>
- Aubry, T. J., Engwell, S. L., Bonadonna, C., Carazzo, G., Scollo, S., Van Eaton, A. R., et al. (2021). The independent volcanic eruption source parameter archive (IVESPA, version 1.0): A new observational database to support explosive eruptive column model validation and development. *Journal of Volcanology and Geothermal Research*, 417, 107295. <https://doi.org/10.1016/j.jvolgeores.2021.107295>
- Aubry, T. J., Engwell, S. L., Bonadonna, C., Mastin, L. G., Carazzo, G., Van Eaton, A. R., et al. (2023). New insights into the relationship between mass eruption rate and volcanic column height based on the IVESPA data set. *Geophysical Research Letters*, 50(14), e2022GL102633. <https://doi.org/10.1029/2022GL102633>
- Beckett, F. M., Bensimon, D., Crawford, A., Deslandes, M., Guidard, V., Hort, M. C., et al. (2024). VAAC model setup tables 2023. <https://doi.org/10.5281/zenodo.10671098>
- Beckett, F. M., Witham, C. S., Hort, M. C., Stevenson, J. A., Bonadonna, C., & Millington, S. C. (2015). Sensitivity of dispersion model forecasts of volcanic ash clouds to the physical characteristics of the particles. *Journal of Geophysical Research: Atmospheres*, 120(22), 11636–11652. <https://doi.org/10.1002/2015JD023609>
- Beckett, F. M., Witham, C. S., Leadbetter, S. J., Crocker, R., Webster, H. N., Hort, M. C., et al. (2020). Atmospheric dispersion modelling at the London VAAC: A review of developments since the 2010 eyjafjallajökull volcano ash cloud. *Atmosphere*, 11(4), 352. <https://doi.org/10.3390/atmos11040352>
- Biass, S., Bonadonna, C., Connor, L., & Connor, C. (2016). TephraProb: A matlab package for probabilistic hazard assessments of tephra fallout. *Journal of Applied Volcanology*, 5(1), 10. <https://doi.org/10.1186/s13617-016-0050-5>
- Bonadonna, C., Macedonio, G., & Sparks, R. S. J. (2002a). Numerical modelling of tephra fallout associated with dome collapses and Vulcanian explosions: Application to hazard assessment on Montserrat. *Geological Society, London, Memoirs*, 21(1), 517–537. <https://doi.org/10.1144/GSL.MEM.2002.021.01.23>

Acknowledgments

The authors would like to acknowledge the Engineering & Physical Sciences Research Council (EPSRC) who funded this research (Grant reference EP/X525583/1). TJJ was also supported by a UK Research and Innovation (UKRI) Future Leaders Fellowship (Grant reference MR/W009781/1). The authors want to thank Nicola Stebbing from the Met Office, who kindly supplied a python script for the plume area overlap calculation (FMS) and supported in the application to our data set, as well as the whole V&C group members at the Met Office for their support on NAME and technical-related questions. Matthew Hort from the Met Office contributed with an inspiring conversation on the grid length resolutions. SLE was supported by the NC-ODA grant NE/R000069/1: Geoscience for Sustainable Futures and published with permission of the CEO, British Geological Survey. We would like to acknowledge Sarah Millington and Symeon Makris from the Met Office and BGS, respectively, for their internal reviews. We also thank our journal reviewers Larry Mastin and Alice Crawford for useful comments that improved this paper.

- Bonadonna, C., Mayberry, G. C., Calder, E. S., Sparks, R. S. J., Choux, C., Jackson, P., et al. (2002b). Tephra fallout in the eruption of Soufrière hills volcano, Montserrat. In *Geological Society, London, Memoirs*, T. H. Druitt & B. P. Kokelaar (Eds.), *The Eruption of Soufrière Hills Volcano, Montserrat from 1995 to 1999* (Vol. 21(1), pp. 483–516). <https://doi.org/10.1144/GSL.MEM.2002.021.01.22>
- Bonadonna, C., & Phillips, J. C. (2003). Sedimentation from strong volcanic plumes. *Journal of Geophysical Research*, *108*(B7), 2340. <https://doi.org/10.1029/2002JB002034>
- Brown, A., Milton, S., Cullen, M., Golding, B., Mitchell, J., & Shelly, A. (2012). Unified modeling and prediction of weather and climate: A 25-Year journey. *Bulletin of the American Meteorological Society*, *93*(12), 1865–1877. <https://doi.org/10.1175/BAMS-D-12-00018.1>
- Brown, R. J., & Andrews, G. D. M. (2015). Chapter 36—Deposits of pyroclastic density currents. In H. Sigurdsson (Ed.), *The encyclopedia of volcanoes* (2nd ed., pp. 631–648). Academic Press. <https://doi.org/10.1016/B978-0-12-385938-9.00036-5>
- Bursik, M. (2001). Effect of wind on the rise height of volcanic plumes. *Geophysical Research Letters*, *28*(18), 3621–3624. <https://doi.org/10.1029/2001GL013393>
- Bursik, M., & Woods, A. W. (1996). The dynamics and thermodynamics of large ash flows. *Bulletin of Volcanology*, *58*(2), 175–193. <https://doi.org/10.1007/s004450050134>
- Calder, E. S., Sparks, R. S. J., & Woods, A. W. (1997). Dynamics of co-ignimbrite plumes generated from pyroclastic flows of Mount St. Helens (7 August 1980). *Bulletin of Volcanology*, *58*(6), 432–440. <https://doi.org/10.1007/s004450050151>
- Carey, S., & Sparks, R. S. J. (1986). Quantitative models of the fallout and dispersal of tephra from volcanic eruption columns. *Bulletin of Volcanology*, *48*(2), 109–125. <https://doi.org/10.1007/BF01046546>
- Charbonnier, S. J., & Gertisser, R. (2008). Field observations and surface characteristics of pristine block-and-ash flow deposits from the 2006 eruption of Merapi volcano, Java, Indonesia. *Journal of Volcanology and Geothermal Research*, *177*(4), 971–982. <https://doi.org/10.1016/j.jvolgeores.2008.07.008>
- Constantinescu, R., Hopulele-Gligor, A., Connor, C. B., Bonadonna, C., Connor, L. J., Lindsay, J. M., et al. (2021). The radius of the umbrella cloud helps characterize large explosive volcanic eruptions. *Communications Earth and Environment*, *2*(1), 3. <https://doi.org/10.1038/s43247-020-00078-3>
- Dacre, H. F., Grant, A. L. M., Hogan, R. J., Belcher, S. E., Thomson, D. J., Devenish, B. J., et al. (2011). Evaluating the structure and magnitude of the ash plume during the initial phase of the 2010 Eyjafjallajökull eruption using LiDAR observations and NAME simulations. *Journal of Geophysical Research*, *116*(D20), D00U03. <https://doi.org/10.1029/2011JD015608>
- Davies, T., Cullen, M. J. P., Malcolm, A. J., Mawson, M. H., Staniforth, A., White, A. A., & Wood, N. (2005). A new dynamical core for the met Office's global and regional modelling of the atmosphere. *Quarterly Journal of the Royal Meteorological Society*, *131*(608), 1759–1782. <https://doi.org/10.1256/qj.04.101>
- Dellino, P., Dioguardi, F., Isaia, R., Sulpizio, R., & Mele, D. (2021). The impact of pyroclastic density currents duration on humans: The case of the AD 79 eruption of Vesuvius. *Scientific Reports*, *11*(1), 4959. <https://doi.org/10.1038/s41598-021-84456-7>
- Devenish, B. J. (2013). Using simple plume models to refine the source mass flux of volcanic eruptions according to atmospheric conditions. *Journal of Volcanology and Geothermal Research*, *256*, 118–127. <https://doi.org/10.1016/j.jvolgeores.2013.02.015>
- Druitt, T. H. (1998). Pyroclastic density currents. *Geological Society, London, Special Publications*, *145*(1), 145–182. <https://doi.org/10.1144/GSL.SP.1996.145.01.08>
- Druitt, T. H., Young, S. R., Baptie, B., Bonadonna, C., Calder, E. S., Clarke, A. B., et al. (2002). Episodes of cyclic vulcanian explosive activity with fountain collapse at Soufrière hills volcano, Montserrat. *Geological Society, London, Memoirs*, *21*(1), 281–306. <https://doi.org/10.1144/GSL.MEM.2002.021.01.13>
- Dufek, J., Esposti Ongaro, T., & Roche, O. (2015). Chapter 35 - Pyroclastic density currents: Processes and models. In H. Sigurdsson (Ed.), *The encyclopedia of volcanoes* (2nd ed., pp. 617–629). Academic Press. <https://doi.org/10.1016/B978-0-12-385938-9.00035-3>
- Dürig, T., Gudmundsson, M. T., Dioguardi, F., Woodhouse, M., Björnsson, H., Barsotti, S., et al. (2018). REFIR - A multi-parameter system for near real-time estimates of plume-height and mass eruption rate during explosive eruptions. *Journal of Volcanology and Geothermal Research*, *360*, 61–83. <https://doi.org/10.1016/j.jvolgeores.2018.07.003>
- Engwell, S. L., de' Michieli Vitturi, M., Esposti Ongaro, T., & Neri, A. (2016). Insights into the formation and dynamics of coignimbrite plumes from one-dimensional models. *Journal of Geophysical Research: Solid Earth*, *121*(6), 4211–4231. <https://doi.org/10.1002/2016JB012793>
- Engwell, S. L., & Eychenne, J. (2016). Chapter 4—Contribution of fine ash to the atmosphere from plumes associated with pyroclastic density currents. In S. Mackie, K. Cashman, H. Ricketts, A. Rust, & M. Watson (Eds.), *Volcanic ash* (pp. 67–85). Elsevier. <https://doi.org/10.1016/B978-0-08-100405-0.00007-0>
- Eychenne, J., & Engwell, S. L. (2022). The grain size of volcanic fall deposits: Spatial trends and physical controls. *GSA Bulletin*, *135*(7–8), 1844–1858. <https://doi.org/10.1130/B36275.1>
- Fisher, R. V., Glicken, H. X., & Hoblitt, R. P. (1987). 1980, Mount St. Helens deposits in south coldwater creek, Washington. *Journal of Geophysical Research*, *92*(B10), 10267–10283. <https://doi.org/10.1029/JB092iB10p10267>
- Folch, A., Costa, A., & Basart, S. (2012). Validation of the FALL3D ash dispersion model using observations of the 2010 Eyjafjallajökull volcanic ash clouds. *Atmospheric Environment*, *48*, 165–183. <https://doi.org/10.1016/j.atmosenv.2011.06.072>
- Giordano, G., & Cas, R. A. F. (2021). Classification of ignimbrites and their eruptions. *Earth-Science Reviews*, *220*, 103697. <https://doi.org/10.1016/j.earscirev.2021.103697>
- Global Volcanism Program. (2024). *Volcanoes of the World* (no. Hekla (372070); version 5.1.7) [Dataset]. Distributed by Smithsonian Institution, compiled by Venzke, E. <https://doi.org/10.5479/si.GVP.VOTW5-2024.5.2>
- Hagenbourger, M., Beckett, F. B., Jones, T. J., & Engwell, S. L. (2025). Supporting information: Modelling the transport and dispersion of volcanic co-PDC ash clouds using NAME: An evaluation of source geometry and mass eruption rate (version NAME III, v.8.5) [Computer software]. *Zenodo*. <https://doi.org/10.5281/zenodo.15084579>
- Harvey, N. J., Huntley, N., Dacre, H. F., Goldstein, M., Thomson, D., & Webster, H. (2018). Multi-level emulation of a volcanic ash transport and dispersion model to quantify sensitivity to uncertain parameters. *Natural Hazards and Earth System Sciences*, *18*(1), 41–63. <https://doi.org/10.5194/nhess-18-41-2018>
- Herzog, M., & Graf, H.-F. (2010). Applying the three-dimensional model ATHAM to volcanic plumes: Dynamic of large co-ignimbrite eruptions and associated injection heights for volcanic gases. *Geophysical Research Letters*, *37*(19), L19807. <https://doi.org/10.1029/2010GL044986>
- Holasek, R. E., & Self, S. (1995). GOES weather satellite observations and measurements of the May 18, 1980, Mount St. Helens eruption. *Journal of Geophysical Research*, *100*(B5), 8469–8487. <https://doi.org/10.1029/94JB03137>
- Jones, A., Thomson, D., Hort, M., & Devenish, B. (2007). The U.K. met office's next-generation atmospheric dispersion model, NAME III. In C. Borrego & A.-L. Norman (Eds.), *Air pollution modeling and its application XVII* (pp. 580–589). Springer, US. https://doi.org/10.1007/978-0-387-68854-1%255C_62

- Jones, T. J., Beckett, F., Bernard, B., Breard, E. C. P., Dioguardi, F., Dufek, J., et al. (2023). Physical properties of pyroclastic density currents: Relevance, challenges and future directions. *Frontiers in Earth Science*, *11*, 1218645. <https://doi.org/10.3389/feart.2023.1218645>
- Lube, G., Breard, E. C. P., Esposti-Ongaro, T., Dufek, J., & Brand, B. (2020). Multiphase flow behaviour and hazard prediction of pyroclastic density currents. *Nature Reviews Earth and Environment*, *1*(7), 348–365. <https://doi.org/10.1038/s43017-020-0064-8>
- Marti, A., Folch, A., Costa, A., & Engwell, S. L. (2016). Reconstructing the plinian and co-ignimbrite sources of large volcanic eruptions: A novel approach for the Campanian Ignimbrite. *Scientific Reports*, *6*(1), 21220. <https://doi.org/10.1038/srep21220>
- Mastin, L. G., Carey, S. N., Van Eaton, A. R., Eycheenne, J., & Sparks, R. S. J. (2022). Understanding and modeling tephra transport: Lessons learned from the 18 May 1980 eruption of Mount St. Helens. *Bulletin of Volcanology*, *85*(1), 4. <https://doi.org/10.1007/s00445-022-01613-0>
- Mastin, L. G., Guffanti, M., Servranckx, R., Webley, P., Barsotti, S., Dean, K., et al. (2009). A multidisciplinary effort to assign realistic source parameters to models of volcanic ash-cloud transport and dispersion during eruptions. *Journal of Volcanology and Geothermal Research*, *186*(1–2), 10–21. <https://doi.org/10.1016/j.jvolgeores.2009.01.008>
- Mastin, L. G., & Van Eaton, A. R. (2020). Comparing simulations of umbrella-cloud growth and ash transport with observations from Pinatubo, kelud, and calbuco volcanoes. *Atmosphere*, *11*(10), 1038. Article 10. <https://doi.org/10.3390/atmos11101038>
- Michol, K. A., Russell, J. K., & Andrews, G. D. M. (2008). Welded block and ash flow deposits from Mount Meager, British Columbia, Canada. *Journal of Volcanology and Geothermal Research*, *169*(3), 121–144. <https://doi.org/10.1016/j.jvolgeores.2007.08.010>
- Morton, B. R., Taylor, G. I., & Turner, J. S. (1956). Turbulent gravitational convection from maintained and instantaneous sources. *Proceedings of the Royal Society of London. Series A. Mathematical and Physical Sciences*, *234*(1196), 1–23. <https://doi.org/10.1098/rspa.1956.0011>
- Neal, R., Fereday, D., Crocker, R., & Comer, R. E. (2016). A flexible approach to defining weather patterns and their application in weather forecasting over Europe. *Meteorological Applications*, *23*(3), 389–400. <https://doi.org/10.1002/met.1563>
- Neri, A., Di Muro, A., & Rosi, M. (2002). Mass partition during collapsing and transitional columns by using numerical simulations. *Journal of Volcanology and Geothermal Research*, *115*(1), 1–18. [https://doi.org/10.1016/S0377-0273\(01\)00304-3](https://doi.org/10.1016/S0377-0273(01)00304-3)
- Neri, A., Esposti Ongaro, T., Macedonio, G., & Gidaspow, D. (2003). Multiparticle simulation of collapsing volcanic columns and pyroclastic flow. *Journal of Geophysical Research*, *108*(B4), 2202. <https://doi.org/10.1029/2001JB000508>
- Pardini, F., Barsotti, S., Bonadonna, C., de' Michieli Vitturi, M., Folch, A., Mastin, L., et al. (2024). Dynamics, monitoring, and forecasting of tephra in the atmosphere. *Reviews of Geophysics*, *62*(4), e2023RG000808. <https://doi.org/10.1029/2023RG000808>
- Pelley, R. E., Thomson, D. J., Webster, H. N., Cooke, M. C., Manning, A. J., Witham, C. S., & Hort, M. C. (2021). A near-real-time method for estimating volcanic ash emissions using satellite retrievals. *Atmosphere*, *12*(12), 1573. <https://doi.org/10.3390/atmos12121573>
- Pioli, L., Bonadonna, C., & Pistolesi, M. (2019). Reliability of total grain-size distribution of tephra deposits. *Scientific Reports*, *9*(1), 10006. <https://doi.org/10.1038/s41598-019-46125-8>
- Pioli, L., & Harris, A. J. L. (2019). Real-time geophysical monitoring of particle size distribution during volcanic explosions at Stromboli Volcano (Italy). *Frontiers in Earth Science*, *7*, 52. <https://doi.org/10.3389/feart.2019.00052>
- Prata, F., Prata, A. T., Tanner, R., Grainger, R. G., Borgas, M., & Aubry, T. J. (2025). The radial spreading of volcanic umbrella clouds deduced from satellite measurements. *Volcanica*, *8*(1), 1–29. <https://doi.org/10.30909/vol.08.01.0129>
- Rolph, G. D., Ngan, F., & Draxler, R. R. (2014). Modeling the fallout from stabilized nuclear clouds using the HYSPLIT atmospheric dispersion model. *Journal of Environmental Radioactivity*, *136*, 41–55. <https://doi.org/10.1016/j.jenvrad.2014.05.006>
- Rosi, M., Bertagnini, A., Harris, A. J. L., Pioli, L., Pistolesi, M., & Ripepe, M. (2006). A case history of paroxysmal explosion at Stromboli: Timing and dynamics of the April 5, 2003 event. *Earth and Planetary Science Letters*, *243*(3), 594–606. <https://doi.org/10.1016/j.epsl.2006.01.035>
- Saint, C., Beckett, F. M., Dioguardi, F., Kristiansen, N., & Tubbs, R. N. (2024). Using simulated radiances to understand the limitations of satellite-retrieved volcanic ash data and the implications for volcanic ash cloud forecasting. *Journal of Geophysical Research: Atmospheres*, *129*(23), e2024JD041112. <https://doi.org/10.1029/2024JD041112>
- Sigurdsson, H., & Carey, S. (1989). Plinian and co-ignimbrite tephra fall from the 1815 eruption of Tambora volcano. *Bulletin of Volcanology*, *51*(4), 243–270. <https://doi.org/10.1007/BF01073515>
- Sparks, R. S. J. (1986). The dimensions and dynamics of volcanic eruption columns. *Bulletin of Volcanology*, *48*(1), 3–15. <https://doi.org/10.1007/BF01073509>
- Sparks, R. S. J., Bursik, M. I., Carey, S. N., Gilbert, J. S., Glaze, L. S., Sigurdsson, H., & Woods, A. W. (1997). *Volcanic plumes*. Wiley.
- Sparks, R. S. J., Moore, J. G., & Rice, C. J. (1986). The initial giant umbrella cloud of the May 18th, 1980, explosive eruption of Mount St. Helens. *Journal of Volcanology and Geothermal Research*, *28*(3), 257–274. [https://doi.org/10.1016/0377-0273\(86\)90026-0](https://doi.org/10.1016/0377-0273(86)90026-0)
- Sulpizio, R., Capra, L., Sarocchi, D., Saucedo, R., Gavilanes-Ruiz, J. C., & Varley, N. R. (2010). Predicting the block-and-ash flow inundation areas at Volcán de Colima (Colima, Mexico) based on the present day (February 2010) status. *Journal of Volcanology and Geothermal Research*, *193*(1), 49–66. <https://doi.org/10.1016/j.jvolgeores.2010.03.007>
- Ui, T., Matsuwo, N., Sumita, M., & Fujinawa, A. (1999). Generation of block and ash flows during the 1990–1995 eruption of Unzen volcano, Japan. *Journal of Volcanology and Geothermal Research*, *89*(1), 123–137. [https://doi.org/10.1016/S0377-0273\(98\)00128-0](https://doi.org/10.1016/S0377-0273(98)00128-0)
- Walters, D., Baran, A. J., Boutle, I., Brooks, M., Eamshaw, P., Edwards, J., et al. (2019). The met office unified model global atmosphere 7.0/7.1 and JULES global land 7.0 configurations. *Geoscientific Model Development*, *12*(5), 1909–1963. <https://doi.org/10.5194/gmd-12-1909-2019>
- Warner, S., Platt, N., & Heagy, J. F. (2004). User-oriented two-dimensional measure of effectiveness for the evaluation of transport and dispersion models. *Journal of Applied Meteorology*, *43*(1), 58–73. [https://doi.org/10.1175/1520-0450\(2004\)043<0058:UTMOEF>2.0.CO;2](https://doi.org/10.1175/1520-0450(2004)043<0058:UTMOEF>2.0.CO;2)
- Watanabe, K., Ono, K., Sakaguchi, K., Takada, A., & Hoshizumi, H. (1999). Co-ignimbrite ash-fall deposits of the 1991 eruptions of Fugen-dake, Unzen Volcano, Japan. *Journal of Volcanology and Geothermal Research*, *89*(1), 95–112. [https://doi.org/10.1016/S0377-0273\(98\)00126-7](https://doi.org/10.1016/S0377-0273(98)00126-7)
- Webster, H. N., Thomson, D. J., Johnson, B. T., Heard, I. P. C., Turnbull, K., Marengo, F., et al. (2012). Operational prediction of ash concentrations in the distal volcanic cloud from the 2010 Eyjafjallajökull eruption. *Journal of Geophysical Research*, *117*(D20). <https://doi.org/10.1029/2011JD016790>
- Webster, H. N., Devenish, B. J., Mastin, L. G., Thomson, D. J., & Van Eaton, A. R. (2020). Operational modelling of umbrella cloud growth in a lagrangian volcanic ash transport and dispersion model. *Atmosphere*, *11*(2), 200. Article 2. <https://doi.org/10.3390/atmos11020200>
- Webster, H. N., Whitehead, T., & Thomson, D. J. (2018). Parameterizing unresolved mesoscale motions in atmospheric dispersion models. *Journal of Applied Meteorology and Climatology*, *57*(3), 645–657. <https://doi.org/10.1175/JAMC-D-17-0075.1>
- Wilkins, K. L., Watson, I. M., Kristiansen, N. I., Webster, H. N., Thomson, D. J., Dacre, H. F., & Prata, A. J. (2016). Using data insertion with the NAME model to simulate the 8 May 2010 Eyjafjallajökull volcanic ash cloud. *Journal of Geophysical Research: Atmospheres*, *121*(1), 306–323. <https://doi.org/10.1002/2015JD023895>
- Wilson, L., Sparks, R. S. J., Huang, T. C., & Watkins, N. D. (1978). The control of volcanic column heights by eruption energetics and dynamics. *Journal of Geophysical Research*, *83*(B4), 1829–1836. <https://doi.org/10.1029/JB083iB04p01829>

- Witham, C., Webster, H., Hort, M., Jones, A., & Thomson, D. (2012). Modelling concentrations of volcanic ash encountered by aircraft in past eruptions. *Atmospheric Environment*, *48*, 219–229. <https://doi.org/10.1016/j.atmosenv.2011.06.073>
- Woods, A. W., & Kienle, J. (1994). The dynamics and thermodynamics of volcanic clouds: Theory and observations from the April 15 and April 21, 1990 eruptions of redoubt volcano, Alaska. *Journal of Volcanology and Geothermal Research*, *62*(1), 273–299. [https://doi.org/10.1016/0377-0273\(94\)90037-X](https://doi.org/10.1016/0377-0273(94)90037-X)
- Woods, A. W., & Wohletz, K. (1991). Dimensions and dynamics of co-ignimbrite eruption columns. *Nature*, *350*(6315), 225–227. <https://doi.org/10.1038/350225a0>
- Zidikheri, M. J., Lucas, C., & Potts, R. J. (2017). Estimation of optimal dispersion model source parameters using satellite detections of volcanic ash. *Journal of Geophysical Research: Atmospheres*, *122*(15), 8207–8232. <https://doi.org/10.1002/2017JD026676>